Master's thesis

NTNU
Norwegian University of Science and Technology
Faculty of Natural Sciences
Department of Physics

Tarjei Heggset

The Effect of the Nuclear Charge Distribution on the Hyperfine Anomaly in Mercury

A Parametric Study with Computational Atomic Physics

Master's thesis in Technical Physics
Supervisor: Rolf Jonas Persson
June 2020

NTNU
Kunnskap for en bedre verden

Tarjei Heggset

The Effect of the Nuclear Charge Distribution on the Hyperfine Anomaly in Mercury

A Parametric Study with Computational Atomic Physics

Master's thesis in Technical Physics
Supervisor: Rolf Jonas Persson
June 2020

Norwegian University of Science and Technology
Faculty of Natural Sciences
Department of Physics

NTNU
Norwegian University of
Science and Technology

Abstract

A parametric study of the Breit-Rosenthal correction between ^{199}Hg and other isotopes was done for the states $6s6p\ ^3P_1$ and $^3P_2$ with the parameter $\delta\langle r_n^2\rangle$ (difference in mean squared radius of nuclear charge distribution) in the range $[-1\,\mathrm{fm}^2, 1\,\mathrm{fm}^2]$. The electronic wave functions were calculated with the multi-configuration Dirac-Hartree-Fock method using the General Relativistic Atomic Structure Package 2018 where a two-parameter Fermi model was used for the nuclear charge distribution. A linear fit $C\delta\langle r_n\rangle$ was made with the results. The factor C was found to differ by approximately 1 % when a large expansion of configurations was used compared with the minimal expansion. The value of the nuclear skin thickness was found to have very little impact on C. C was found to be $-0.1113\,\%\,\mathrm{fm}^{-2}$ for $^3P_1$ and $-0.1164\,\%\,\mathrm{fm}^{-2}$ for $^3P_2$.

Unit System

The system of units used in this report is the Hartree atomic units. In this system the following quantities are defined to be unity:

Electron mass	m_e
Elementary charge	e
Reduced Planck constant	$\hbar$
Inverse Coulomb constant	$4\pi\epsilon_0$

Distances on the nuclear scale are measured in femtometer(fm).

Contents

List of Figures

List of Tables

List of Abbreviations

AS Active Set

ASF Atomic State Function

BR Breit-Rosenthal

BW Bohr-Weisskopf

cc Core-Core

CF Central Field

CG Clebsch-Gordan

CI Configuration Interaction

CSF Configuration State Function

cv Core-Valence

DC Dirac-Coulomb

FS Field Shift

GRASP2018 General Relativistic Atomic Structure Package 2018

hfs Hyperfine Structure

MCDHF Multi-Configuration Dirac-Hartree-Fock

MS Mass Shift

QED Quantum Electrodynamics

RCI	Relativistic Configuration Interaction
rms	Root-mean-square
scf	Self-Consistent Field
TF	Thomas-Fermi
vv	Valence-Valence

Chapter 1

Introduction

The nuclear magnetic moment of nuclei with short lifetimes can be found from spectroscopic measurements of the electronic hyperfine structure when these are compared to those obtained for a more stable reference nucleus for which the magnetic moment is known. The calculations involved are associated with the so-called hyperfine anomaly which introduces some uncertainty. Parts of the uncertainty can be removed if the Breit-Rosenthal correction due to the finite nuclear charge distribution is calculated. The project presented in this report concerns a parametric study of the Breit-Rosenthal corrections for the states $6s6p\ ^3P_1$ and $^3P_2$ between ^{199}Hg and other isotopes. The aim of the project was to estimate the contribution from the Breit-Rosenthal correction to the hyperfine anomaly between unstable isotopes of Hg and the reference isotope ^{199}Hg.

Chapters 2 to 4 concern theoretical considerations of the concepts and methods used in the project. Chapter 5 concerns computations of the electronic wave functions in the reference isotope ^{199}Hg with use of the General Relativistic Atomic Structure Package 2018. The experimentally measured values of the hyperfine structure constants for the states $6s6p\ ^3P_1$ and $^3P_2$ were used in the determination of the wave functions. Chapter 6 concerns the parametric study where the method developed for ^{199}Hg was used to calculate the wave functions with different nuclear radii to model the difference between isotopes. Conclusions based on the results of the study are presented in chapter 7.

Chapter 2

Nuclear Magnetic Dipole Moment

An atomic nucleus possesses a magnetic dipole moment from the spin of the protons and neutrons, and the orbital angular momentum of the protons.

In classical electromagnetism, the magnetic dipole moment $\vec{\mu}$ of a system consisting of a particle with charge q and mass m moving relative to a specific axis is related to its angular momentum $\vec{l}$ by

$$\vec{\mu} = \frac{q}{2m}\vec{l} = \gamma\vec{l}, \tag{2.1}$$

where $\gamma \equiv \frac{q}{2m}$ is the gyromagnetic ratio for the classical system. An example of such a system is presented in Figure 2.1.

In the quantum mechanical description, the nucleus is described by a state vector $|\psi_n\rangle$. For a free nucleus the total angular momentum is conserved and the nuclear state can be described in terms of stationary eigenstates $|I^\pi, M_I\rangle$ [4, p. 67] of the square of the nuclear angular momentum operator $\hat{\vec{I}}^2$ with eigenvalue $I(I+1)$ and the nuclear angular momentum projection operator $\hat{I}_z$ with eigenvalue M_I, where $I \in \{0, 1/2, 1, \ldots\}$ and $M_I \in \{-I, -I+1, \ldots, I\}$. The angular momentum eigenstates have parity $\pi = \pm 1$.

The nuclear magnetic moment is described by a sum over the magnetic moment operators for the nucleons. The connection between a nucleonic angular momentum and the resulting magnetic moment is analogous to the classical system in that they are proportional but with a so-called g-factor multiplied with the classical gyromagnetic ratio to account for anomalies. The nuclear magnetic moment operator becomes [4, p. 75]

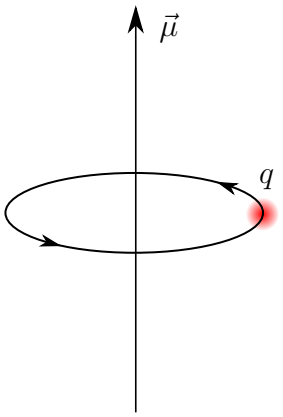

Figure 2.1: Schematic of a particle with charge q moving in a circular motion. According to classical electromagnetism, the system possesses a magnetic dipole moment $\vec{\mu} = q\vec{l}/2m$, where $\vec{l}$ is the angular momentum of the particle w.r.t. the axis through the center of the circle, normal to the plane of motion, and m is the mass of the particle.

$$\hat{\vec{\mu}} = \sum_{i=1}^{A} g_i^l \mu_N \hat{\vec{l}}_i + g_i^s \mu_N \hat{\vec{s}}_i. \tag{2.2}$$

The summation is over the A nucleons where the orbital g-factors g_i^l are 1 for protons and 0 for neutrons, and the spin g-factors g_i^s are approximately 5.5856 for free protons and -3.8263 for free neutrons [4, p. 66]. $\hat{\vec{l}}_i$ and $\hat{\vec{s}}_i$ are the orbital angular momentum and spin operators for nucleon i. μ_N is the nuclear magneton which is a dimensionless quantity with a value of approximately $2.7231 \cdot 10^{-4}$ in the Hartree atomic unit system and is analogous to the classical gyromagnetic ratio in equation 2.1 for the proton.

The magnetic moment μ_I of a nucleus that is described by a state with angular momentum quantum number I is the largest expectation value of the projection of the magnetic moment operator along a specific z-axis and is defined as [4, p. 75]

$$\mu_I = \langle I, M_I = I | \hat{\mu}_z | I, M_I = I \rangle = g_I \mu_N I, \tag{2.3}$$

which also defines the nuclear g-factor g_I.

In the ground state, pairs of protons and pairs of neutrons tend to align with opposite angular momenta. Even numbers of nucleons of the same type

therefore give net contributions of 0 to the magnetic moment. The nuclear magnetic moment can then be assumed to result from the unpaired proton and/or neutron in nuclei where the magnetic moment is non-zero. Theoretical models such as the Schmidt model can be used to make predictions of the factor g_I [18]. However, the theoretically predicted values may not be sufficiently accurate for all types of applications where the value of the nuclear magnetic moment is needed. Accurate measurements of the nuclear magnetic moment is then necessary to provide this information.

Different techniques exist for measuring the nuclear magnetic moment. The conventional and most precise techniques like nuclear magnetic resonance require some minimum lifetime of the nuclei for the measurements to be carried out [24, pp. 12–28]. Some unstable nuclei have too short lifetimes for these techniques to be used. The nuclear magnetic moment of these unstable nuclei can however be inferred by studying the energy spectrum of the electronic system surrounding the nucleus with the use of spectroscopic measurements.

The interactions between the electrons and electromagnetic multipole moments of the nucleus cause the atomic energy spectrum to differ somewhat from that predicted using a point charge model for the nucleus. These correctional interactions are small compared to the point charge Coulomb interactions and they cause relatively small splittings of the energy levels obtained in the point charge model. The energy corrections are typically less than $10\,\mu\text{eV}$ [10, p. 17] which gives a factor of 10^{-5} compared to the typical energies with the point charge which are in the range of eV. The structure of energy levels resulting from the interactions between the electrons and the higher order electromagnetic multipole moments of the nucleus is known as the hyperfine structure (hfs).

Chapter 3

Hyperfine Structure

3.1 Electric Interaction

The electric interaction energy between an atomic nucleus and the surrounding electrons can in a semi-classical picture be described in terms of the Hamiltonian operator

$$\begin{aligned}
\hat{H}_E &= -\sum_{i=1}^{N}\sum_{j=1}^{Z}\frac{1}{|\vec{r_j}-\vec{r_i}|} \\
&= -\sum_{i=1}^{N}\sum_{j=1}^{Z}\sum_{l=0}^{\infty}\frac{r_<^l}{r_>^{l+1}}\sum_{m=-l}^{l}Y_l^{m*}(\theta_i,\phi_i)Y_l^m(\theta_j,\phi_j) \\
&= -\sum_{i=1}^{N}\sum_{j=1}^{Z}\big[\frac{1}{r_i}+\big(\frac{1}{r_j}-\frac{1}{r_i}\big)\Theta(r_j-r_i) \\
&\quad +\sum_{l=1}^{\infty}\frac{r_<^l}{r_>^{l+1}}\sum_{m=-l}^{l}Y_l^{m*}(\theta_i,\phi_i)Y_l^m(\theta_j,\phi_j)\big] \\
&= -\sum_{i=1}^{N}\frac{Z}{r_i}+\hat{H}'_E, \qquad (3.1)
\end{aligned}$$

where the Laplace expansion in terms of the spherical harmonics $Y_l^m(\theta,\phi)$ [8, p. 48] has been used for the inverse distance $|\vec{r_j}-\vec{r_i}|^{-1}$ between electron i and proton j. $r_<$ and $r_>$ are the lesser and greater of the values $r_i=|\vec{r_i}|$ and $r_j=|\vec{r_j}|$. The sum is over the N electrons and Z protons of the atomic

system. $\Theta(x)$ is the Heaviside step function. In the last line the Hamiltonian has been separated into the point nucleus Coulomb potential, also known as the electric monopole term, and a correction term $\hat{H}'_E$. Since the correction term is small compared to the monopole term, the energy corrections can be approximated using first order perturbation theory where the zero-order states are obtained as eigenstates of the Hamiltonian describing the atomic system with a point charge nucleus. If $|\psi_n\rangle$ and $|\psi_e\rangle$ are the zero-order nuclear and electronic states, respectively, the zero-order state of the atomic system can be constructed as a direct product of the nuclear and electronic states since the zero-order Hamiltonian is a sum of operators operating on either the nuclear or the electronic subspaces. The first order energy correction then becomes

$$\begin{aligned}\langle\psi_e|\langle\psi_n|\hat{H}'_E|\psi_n\rangle|\psi_e\rangle =& -\sum_{i=1}^{N}\sum_{j=1}^{Z}\langle\psi_e|\langle\psi_n|\big[\big(\frac{1}{r_j}-\frac{1}{r_i}\big)\Theta(r_j-r_i) \\ &+\sum_{l=1}^{\infty}\frac{r_<^l}{r_>^{l+1}}\sum_{m=-l}^{l}Y_l^{m*}(\theta_i,\phi_i)Y_l^m(\theta_j,\phi_j)\big]|\psi_n\rangle|\psi_e\rangle.\end{aligned} \tag{3.2}$$

The first term in the correction operator $\hat{H}'_E$ is the monopole shift operator that results from the deviation of the potential energy from the monopole term when electron i is closer to the atomic center than proton j. The energy correction from the monopole shift can be estimated to first order as follows.

$$
\begin{aligned}
&- \sum_{i=1}^{N}\sum_{j=1}^{Z} \langle\psi_e|\langle\psi_n|\big(\frac{1}{r_j} - \frac{1}{r_i}\big)\Theta(r_j - r_i)|\psi_n\rangle|\psi_e\rangle \\
&= \sum_{i=1}^{N}\sum_{j=1}^{Z} \int d\vec{r}_i \int d\vec{r}_j \big(\frac{1}{r_i} - \frac{1}{r_j}\big)\Theta(r_j - r_i)|\psi_i(\vec{r}_i)|^2|\psi_j(\vec{r}_j)|^2 \\
&\approx \sum_{i=1}^{N} |\psi_i(0)|^2 \sum_{j=1}^{Z} \int d\vec{r}_j \rho_j(\vec{r}_j) \int d\vec{r}_i \big(\frac{1}{r_i} - \frac{1}{r_j}\big)\Theta(r_j - r_i) \\
&= 4\pi \sum_{i=1}^{N} |\psi_i(0)|^2 \sum_{j=1}^{Z} \int d\vec{r}_j \rho_j(\vec{r}_j) \int_0^{r_j} dr_i \big(r_i - \frac{r_i^2}{r_j}\big) \\
&= \frac{2\pi}{3} \sum_{i=1}^{N} |\psi_i(0)|^2 \sum_{j=1}^{Z} \int d\vec{r}_j \rho_j(\vec{r}_j) r_j^2 \\
&= \frac{2\pi}{3} \sum_{i=1}^{N} |\psi_i(0)|^2 \int d\vec{r} r^2 \sum_{j=1}^{Z} \rho_j(\vec{r}) \\
&= \frac{2\pi Z \langle r_n^2\rangle}{3} \sum_{i=1}^{N} |\psi_i(0)|^2. \qquad (3.3)
\end{aligned}
$$

Here $|\psi_i(\vec{r}_i)|^2$ is the absolute square of the part of the electronic state in the space belonging to electron i and similarly with $|\psi_j(\vec{r}_j)|^2 = \rho_j(\vec{r}_j)$ for the protons. $\langle r_n^2\rangle$ is the expectation value of the square of the radius of the nuclear charge distribution, also known as the mean squared radius. The approximation in line 3 can be done since the electronic wave functions are nearly constant over the typical nuclear distances [6, p. 157]. It is seen from this result that the monopole shift mostly affects electronic wave functions that have a non-zero value at the atomic origin and that the energy correction is proportional to the mean squared radius of the nuclear charge distribution.

3.1.1 Isotope Shift

An electronic energy level transition ν differs somewhat between different isotopes. The difference $\delta\nu_{1,2}$ between isotopes 1 and 2 is known as the isotope shift and can be separated into a shift due to the difference in mass, known as the mass shift (MS) and a shift due to the difference in charge

distribution, known as the field shift (FS). The expression for the isotope shift becomes [12]

$$\delta\nu_{1,2} = \nu_2 - \nu_1 = \delta\nu_{1,2}^{FS} + \delta\nu_{1,2}^{MS}. \tag{3.4}$$

For the investigations of the variation in the hfs among the isotopes only the FS is relevant and the MS will not be discussed further.

To first order, the energy correction from the finite charge distribution is proportional to the mean squared radius, as shown in equation 3.3. The first order approximation to the FS is therefore proportional to the difference in mean squared radius $\delta\langle r_n^2\rangle_{1,2}$ between the isotopes. The significance of corrections from higher order radial moments increases with the nuclear size and can reach up to 10 % of the FS for the heaviest elements [12]. Deviation from the first order approximation can be accounted for using a linear fit $kF\delta\langle r_n^2\rangle_{1,2}$, where the dimensionless factor k can be determined experimentally and $F = 2\pi Z\Delta\rho_e(0)/3$. $\Delta\rho_e(0) = \sum_{i=1}^{N}\Delta|\psi_i(0)|$ is the difference in the electron charge density at the nuclear center between the states associated with the electronic transition.

3.1.2 Higher Order Electric Interactions

The terms in the sum over l in Equation 3.2 are energy corrections from interactions between the electrons and the higher order electric multipole moments of the nucleus. When the nuclear state is an eigenstate $|\boldsymbol{\alpha}; I^\pi, M_I\rangle$ of the total angular momentum and parity operators, which is the case for the ground state, the terms $\langle\boldsymbol{\alpha}; I^\pi, M_I|Y_l^m(\theta_j,\phi_j)|\boldsymbol{\alpha}; I^\pi, M_I\rangle$ are 0 for odd l since they are integrals over the unit sphere of functions of odd parity. Here, $\boldsymbol{\alpha}$ represents additional specifications for the nuclear state.

The typical distances from the atomic origin to the electrons are much larger than those to the nucleons. The typical values of the factors r_j^l/r_i^{l+1} therefore decrease rapidly as l increases. The term with $l = 2$ will then be the dominant higher order correction. This term is associated with the so-called electric quadrupole moment of the nucleus and is usually the only higher order electric interaction that is considered in the study of the hfs.

3.2 Magnetic Interaction

The magnetic interaction between the electrons and the nucleus can be described in terms of the magnetic moment of the nucleons in the presence of the magnetic flux density generated by the orbital motion and spin of the electrons.

The magnetic flux density generated by the orbital motion can be obtained in a semi-classical approach where the Biot-Savart law is used. The current density operator of electron i is $-\delta^3(\vec{r}-\vec{r}_i)\hat{\vec{p}}_i$, where $\hat{\vec{p}}_i$ is the momentum operator. The resulting magnetic flux density at the position of nucleon j due to the orbital motion of electron i is then

$$\hat{\vec{B}}^l_{ij} = -\frac{\mu_0}{4\pi}\frac{(\vec{r_i}-\vec{r_j})\times\hat{\vec{p}}_i}{|\vec{r}_i-\vec{r}_j|^3} = -\frac{\mu_0}{4\pi}\frac{\vec{r}_{ij}\times\hat{\vec{p}}_i}{|\vec{r}_i-\vec{r}_j|^3}, \tag{3.5}$$

where μ_0 is the vacuum susceptibility and $\vec{r}_{ij} \equiv \vec{r}_i - \vec{r}_j$.

The magnetic flux density at the position of nucleon j resulting from the spin of electron i is given by the expression for the magnetic flux density from a magnetic point dipole where the anomalous g-factor $g_s = 2.0023\ldots$ can be used. The expression becomes [11]

$$\hat{\vec{B}}^s_{ij} = -\frac{\mu_0}{4\pi}g_s\mu_B\big(\frac{3\hat{\vec{r}}_{ij}(\hat{\vec{r}}_{ij}\cdot\vec{s}_i)-\vec{s}_i}{|\vec{r}_i-\vec{r}_j|^3} + \frac{8\pi}{3}\hat{\vec{s}}_i\delta^3(\vec{r}_i-\vec{r}_j)\big), \tag{3.6}$$

where $\hat{\vec{r}}_{ij}$ is the unit vector in the direction of $\vec{r}_i-\vec{r}_j$. μ_B is the Bohr magneton which is dimensionless with the value $1/2$ in the Hartree atomic unit system.

The energy associated with the magnetic interactions are described by the Hamiltonian operator

$$\begin{aligned}\hat{H}_M &= \sum_{i=1}^{N}\sum_{j=1}^{A} -\hat{\vec{\mu}}_j\cdot(\hat{\vec{B}}^l_{ij}+\hat{\vec{B}}^s_{ij}) \\ &= \sum_{i=1}^{N}\sum_{j=1}^{A}\frac{\mu_0}{4\pi}\hat{\vec{\mu}}_j\cdot\big(\frac{\vec{r}_{ij}\times\hat{\vec{p}}_i + g_s\mu_B[3\hat{\vec{r}}_{ij}(\hat{\vec{r}}_{ij}\cdot\vec{s}_i)-\vec{s}_i]}{|\vec{r}_i-\vec{r}_j|^3} \\ &\quad + \frac{8\pi g_s\mu_B}{3}\hat{\vec{s}}_i\delta^3(\vec{r}_i-\vec{r}_j)\big),\end{aligned} \tag{3.7}$$

where $\hat{\vec{\mu}}_j$ is the magnetic moment operator for nucleon j from equation 2.2. The factor $|\vec{r}_i - \vec{r}_j|^{-3}$ can be expressed as

$$\frac{1}{|\vec{r}_i - \vec{r}_j|^3} = -\frac{\vec{r}_i}{r_i^2} \cdot \nabla_i \frac{1}{|\vec{r}_i - \vec{r}_j|} = -\frac{1}{r_i} \partial_{r_i} \frac{1}{|\vec{r}_i - \vec{r}_j|} \tag{3.8}$$

which, similarly to the case with the electric interaction, can be expressed with the Laplace expansion as

$$\begin{aligned} -\frac{\partial_{r_i}}{r_i} \frac{1}{|\vec{r}_i - \vec{r}_j|} &= -\frac{\partial_{r_i}}{r_i} \sum_{l=0}^{\infty} \frac{r_<^l}{r_>^{l+1}} \sum_{m=-l}^{l} Y_l^{m*}(\theta_i, \phi_i) Y_l^m(\theta_j, \phi_j) \\ &\approx -\frac{\partial_{r_i}}{r_i} \sum_{l=0}^{\infty} \frac{r_j^l}{r_i^{l+1}} \sum_{m=-l}^{l} Y_l^{m*}(\theta_i, \phi_i) Y_l^m(\theta_j, \phi_j) \\ &= \sum_{l=0}^{\infty} (l+1) \frac{r_j^l}{r_i^{l+3}} \sum_{m=-l}^{l} Y_l^{m*}(\theta_i, \phi_i) Y_l^m(\theta_j, \phi_j). \end{aligned} \tag{3.9}$$

Here the approximation in line number 2 is based on the fact that the distances from the atomic center to the electrons mostly are larger than those to the nucleons.

The terms with odd l in the first order energy correction from the magnetic interaction $\langle \psi_e | \langle \psi_n | \hat{H}_M | \psi_n \rangle | \psi_e \rangle$ almost vanish due to parity of the nuclear state (the nuclear position vector $\vec{r}_j$ in the numerator in equation 3.7 can give relatively small, non-vanishing contributions). The terms with even l correspond to the interactions between the electrons and the odd magnetic multipole moments since the magnetic moment and magnetic flux density are (axial)vector-like quantities. Since the contributions from the different magnetic multipole moments decrease rapidly with increasing values of l, the term with $l = 0$ is usually the only term that is considered. This term is associated with the magnetic dipole moment of the nucleus μ_I from equation 2.3 and can therefore be useful to obtain information about this quantity experimentally.

3.2.1 Magnetic Point Dipole Approximation

The term $\vec{r}_{ij} \times \hat{\vec{p}}_i = \hat{\vec{l}}_i - \vec{r}_j \times \hat{\vec{p}}_i$ can be approximated by $\hat{\vec{l}}_i$ in the first order energy correction from the magnetic interactions since $\vec{r}_j \times \hat{\vec{p}}_i$ for the most

part is significantly smaller than $\hat{\vec{l}}_i$ while it also cancels out during integration over the nuclear coordinates for a nuclear parity state. Similarly, the term $\vec{r}_{ij}(\vec{r}_{ij} \cdot \hat{\vec{s}}_i)$ can be approximated with $\hat{\vec{r}}_i(\hat{\vec{r}}_i \cdot \hat{\vec{s}}_i)$ where $\hat{\vec{r}}_i$ is the radial unit vector for electron i (however, there will be terms squared in the nucleon coordinates that do not vanish under integration of the nuclear coordinates).

Since the electronic wave functions are approximately constant over the nuclear coordinates, the factor $\delta^3(\vec{r}_i - \vec{r}_j)$ in the so-called contact term can be approximated with $\delta^3(\vec{r}_i)$. Using these approximations along with the magnetic dipole term ($l = 0$) in the Laplace expansion, the resulting approximate Hamiltonian describes a system where the nucleus is modeled with a magnetic point dipole at the center and is given by

$$\begin{aligned} \hat{H}_{p.d.} &= -\hat{\vec{\mu}} \cdot \hat{\vec{B}} \\ &= \frac{\mu_0}{4\pi} \hat{\vec{\mu}} \cdot \sum_{i=1}^{N} \Big[\frac{\hat{\vec{l}}_i}{r_i^3} + \frac{g_s \mu_B [3\hat{\vec{r}}_i(\hat{\vec{r}}_i \cdot \hat{\vec{s}}_i) - \hat{\vec{s}}_i]}{r_i^3} + \frac{8\pi g_s \mu_B}{3} \hat{\vec{s}}_i \delta^3(\vec{r}_i) \Big], \end{aligned} \tag{3.10}$$

where $\hat{\vec{\mu}}$ is the nuclear magnetic moment operator from equation 2.2 and $\hat{\vec{B}}$ is the operator for the magnetic flux density at the center of the nucleus from the electrons. A simplified schematic of the point dipole interaction is presented in Figure 3.1.

3.2.2 Magnetic Hyperfine Structure Constant

The magnetic dipole hyperfine interaction can be parameterized with the magnetic hyperfine structure constant A [10, p. 18] as

$$\hat{H}_{hfs} = A \hat{\vec{I}} \cdot \hat{\vec{J}}, \tag{3.11}$$

where $\hat{\vec{I}}$ and $\hat{\vec{J}}$ are the total angular momentum operators for the nuclear and electronic systems, respectively.

The total angular momentum operator for the atomic system is $\hat{\vec{F}} = \hat{\vec{I}} + \hat{\vec{J}}$. In a free atomic system the total angular momentum is conserved. The system can then be described in terms of stationary eigenstates of the operators $\hat{\vec{F}}^2$ and $\hat{F}_z$ with the corresponding eigenvalues $F(F+1)$ with $F \in \{|I-J|, |I-J|+1, \ldots, I+J\}$ and $M_F \in \{-F, -F+1, \ldots, F\}$, respectively.

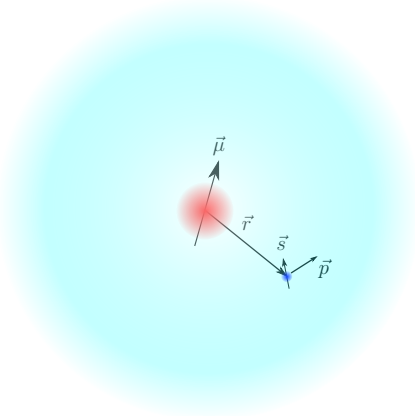

Figure 3.1: Schematic of the magnetic interaction between the magnetic moment of the nucleus, $\vec{\mu}$, and the spin $\vec{s}$ and motion with momentum $\vec{p}$ of an electron. The light blue area represents the electron cloud and the dark blue dot represents a point in the electron cloud at position $\vec{r}$. The red dot in the center represents the nucleus. Proportions in the sketch are not accurate. The vectors are symbolic as the quantities $\vec{\mu}$, $\vec{s}$ and $\vec{l} = \vec{r} \times \vec{p}$ follow the Heisenberg uncertainty principle.

These states can be expanded in terms of direct products of the angular momentum eigenstates of the nuclear and electronic subsystems with the Clebsch-Gordan (CG) expansion

$$|\boldsymbol{\alpha} JI; F, M_F\rangle = \sum_{M_I} \sum_{M_J} C^{F,M_F}_{M_I,M_J} |\boldsymbol{\alpha}_n; I, M_I\rangle |\boldsymbol{\alpha}_e; J, M_J\rangle, \tag{3.12}$$

where $\boldsymbol{\alpha}_n$, $\boldsymbol{\alpha}_e$ and $\boldsymbol{\alpha}$ represent the sets of additional quantum numbers describing the nuclear, electronic and total states, respectively. The factors $C^{F,M_F}_{M_I,M_J}$ are known as the Clebsch-Gordan coefficients [8, p. 55]. The total states are then also eigenstates of the operators $\hat{\vec{I}}^2$ and $\hat{\vec{J}}^2$ with eigenvalues $I(I+1)$ and $J(J+1)$, respectively.

The operator $\hat{\vec{F}}^2$ can be expressed as

$$\hat{\vec{F}}^2 = (\hat{\vec{I}} + \hat{\vec{J}})^2 = (\hat{\vec{I}}^2 + \hat{\vec{J}}^2 + 2\hat{\vec{I}} \cdot \hat{\vec{J}}) = [I(I+1) + J(J+1)] + 2\hat{\vec{I}} \cdot \hat{\vec{J}} = F(F+1), \tag{3.13}$$

so that the operator $\hat{H}_{hfs}$ in equation 3.11 can be expressed as

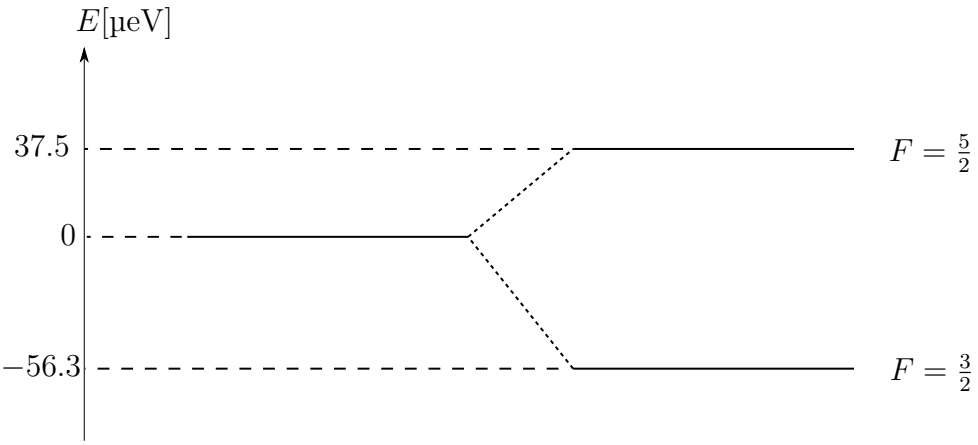

Figure 3.2: Energy level diagram for the hyperfine structure of $6s6p\ ^3P_2$ in ^{199}Hg from the magnetic dipole interaction.

$$\frac{A}{2}(F(F+1) - I(I+1) - J(J+1)) \tag{3.14}$$

when operating on the total states.

The energy difference between two states with quantum numbers F and $F-1$ then becomes

$$\Delta E_{F,F-1} = \frac{A}{2}[F(F+1) - (F-1)F] = AF, \tag{3.15}$$

which determines how an energy level in the unperturbed system is split into $2\min(I,J)$ energy levels in the first order perturbation.

As an example, the hfs constant for the electronic state $6s6p\ ^3P_2$ in ^{199}Hg has been experimentally measured to be 9066.6236(20) MHz [19]. This corresponds to an energy of approximately 37.5 μeV. The ground state of the nucleus has angular momentum $I = 1/2$. With $J = 2$, the possible values of F are 3/2 and 5/2. The energy level splitting corresponding to these two F states are shown in Figure 3.2 where the middle line represents the energy level of $6s6p\ ^3P_2$ in the unperturbed system which has been set to 0 as a reference energy in the diagram.

If $F = M_F = I + J$, the only possible term in the CG expansion is $|\boldsymbol{\alpha}_n; I, I\rangle|\boldsymbol{\alpha}_e; J, J\rangle$. If the electronic states and the nuclear magnetic moment are known, the hfs constant for the point dipole approximation can be calculated by

$$
\begin{aligned}
A_{p.d.} &= \frac{\langle \boldsymbol{\alpha}_e; J, J | \langle \boldsymbol{\alpha}_n; I, I | \hat{H}_{p.d.} | \boldsymbol{\alpha}_n; I, I \rangle | \boldsymbol{\alpha}_e; J, J \rangle}{IJ} \\
&= \frac{\mu_I}{I} \frac{\langle \boldsymbol{\alpha}_e; J, J | \hat{B}_z | \boldsymbol{\alpha}_e; J, J \rangle}{J} \\
&= g_I \mu_N \frac{\langle \boldsymbol{\alpha}_e; J, J | \hat{B}_z | \boldsymbol{\alpha}_e; J, J \rangle}{J},
\end{aligned} \tag{3.16}
$$

where the definitions of the nuclear magnetic moment μ_I and nuclear g-factor g_I in equation 2.3 have been used and $\hat{B}_z$ is the z component of the operator $\hat{\vec{B}}$ in equation 3.10.

3.3 Hyperfine Anomaly

When considering a nuclear model with a point magnetic dipole moment, the deviation of the hfs constant for a finite charge distribution from that of a point charge is caused by deviations in the electronic wave functions and is parameterized with the Breit-Rosenthal (BR) correction ϵ_{BR} [23, p. 2] defined by

$$
A_{p.d.} = A_p(1 + \epsilon_{BR}), \tag{3.17}
$$

where A_p is the hfs constant with a point charge nucleus.

Due to the finite distribution of the nuclear magnetic moment, the hfs constant deviates from that of the point-dipole approximation. This deviation is parameterized with the Bohr-Weisskopf (BW) correction ϵ_{BW} [23, p. 2] defined by

$$
A = A_{p.d.}(1 + \epsilon_{BW}). \tag{3.18}
$$

The ratio between the hfs constants for the same electron configuration in two different isotopes then becomes [23, p. 3]

$$
\begin{aligned}
\frac{A^{(1)}}{A^{(2)}} &= \frac{g_I^{(1)}(1 + \epsilon_{BR}^{(1)})(1 + \epsilon_{BW}^{(1)})}{g_I^{(2)}(1 + \epsilon_{BR}^{(2)})(1 + \epsilon_{BW}^{(2)})} \approx \frac{g_I^{(1)}}{g_I^{(2)}}(1 + \epsilon_{BR}^{(1)} - \epsilon_{BR}^{(2)} + \epsilon_{BW}^{(1)} - \epsilon_{BW}^{(2)}) \\
&= \frac{g_I^{(1)}}{g_I^{(2)}}(1 + {}^1\Delta_{BR}^2 + {}^1\Delta_{BW}^2) = \frac{g_I^{(1)}}{g_I^{(2)}}(1 + {}^1\Delta^2),
\end{aligned} \tag{3.19}
$$

$^{199}\Delta^{195}$[%]	−0.1470(9), [23, p. 14]
$^{199}\Delta^{197}$[%]	−0.0778(7), [23, p. 14]
$^{199}\Delta^{201}$[%]	−0.1467(6), [23, p. 14]

Table 3.1: Hyperfine anomaly between some isotopes of Hg with the electronic state $6s6p\ ^3P_1$.

where the approximation can be done since the corrections are relatively small. This defines the BR and BW contributions $^1\Delta^2_{BR}$ and $^1\Delta^2_{BW}$ to the hyperfine anomaly $^1\Delta^2$ between isotopes 1 and 2. The ratio with a reference isotope is used since uncertainties in calculations of $A_{p.d.}$ cancel [23, p. 2]. The value of the magnetic moment of an unstable nucleus can then be obtained from that of a more stable isotope for which the magnetic moment is known if the hyperfine anomaly is known. If the hyperfine anomaly is not known, this would introduce an uncertainty for the calculation of the unknown magnetic moment. Examples of the hyperfine anomalies between ^{199}Hg and three different isotopes are shown in Table 3.1. The hyperfine anomaly is typically on the order of 1 % or less, but can reach up to 10 % in some cases [23].

The BR contribution can in principle be calculated with ab initio methods using experimental data of the structure of the nuclear charge distribution. Calculation of the BW contribution is often not possible due to the lack of knowledge of the distribution of nuclear magnetization [23].

For most isotopes, the BR effect is considered to be negligible compared to the BW effect. But for nuclei that are very similar the BR effect will dominate [23]. In these cases the calculation of the BR effect could significantly reduce the uncertainty associated with the hyperfine anomaly.

3.4 Computation of the Breit-Rosenthal Effect

The significance of the BR effect can be studied with computational ab initio methods such as the multi-configuration Dirac-Hartree-Fock (MCDHF) method. By variation of the nuclear charge distribution for the potential energy of the electrons, the corresponding variation in the calculated hfs constant can be found for a point dipole approximation, as in equation 3.16.

The variation in nuclear charge distribution mostly affects only the $s_{1/2}$ and $p_{1/2}$ electrons since they are the only ones with a non-zero probability density at the nuclear center, which is required for the nuclear charge distribution to perturb the states in a first order approximation as shown in equation 3.3.

A calculation similar to the one for the monopole shift can be done to estimate how the hfs constant will change when the nuclear charge distribution is varied. The first order corrections to the zero-order electronic state $|\psi_\alpha\rangle$ due to the monopole shift operator $\hat{H}_{mps} = (1/r_i - 1/r_j)\Theta(r_j - r_i)$ is given by

$$\begin{aligned} |\psi_\alpha\rangle^{(1)} &= \sum_{\beta\neq\alpha} \frac{\langle\psi_\beta|\hat{H}_{mps}|\psi_\alpha\rangle}{E_\alpha - E_\beta}|\psi_\beta\rangle \approx \sum_{\beta\neq\alpha} \frac{2\pi Z\langle r_n^2\rangle \sum_{i=1}^{N}\psi^*_{\beta,i}(0)\psi_{\alpha,i}(0)}{3(E_\alpha - E_\beta)}|\psi_\beta\rangle \\ &= \langle r_n^2\rangle \sum_{\beta\neq\alpha} c_{\alpha,\beta}|\psi_\beta\rangle, \end{aligned} \tag{3.20}$$

where the summation index β represents zero-order electronic states for which the matrix elements $\langle\psi_\beta|\hat{H}_{mps}|\psi_\alpha\rangle$ are non-zero and that are different from $|\psi_\alpha\rangle$. Since the monopole shift is relatively small, the BR correction from equation 3.18 can be approximated by

$$\begin{aligned} \epsilon_{BR} &= \frac{A_{p.d.}}{A_p} - 1 \\ &\approx \frac{1}{A_p}(\langle\psi_\alpha| + \langle r_n^2\rangle \sum_\beta c^*_{\alpha,\beta}\langle\psi_\beta|)\frac{\mu_I}{I}\frac{\hat{\vec{B}}}{J}(|\psi_\alpha\rangle + \langle r_n^2\rangle \sum_\beta c_{\alpha,\beta}|\psi_\beta\rangle) - 1 \\ &\approx 1 + \frac{\langle r_n^2\rangle\mu_I}{IJA_p}\sum_\beta (c^*_{\alpha,\beta}\langle\psi_\beta|\hat{\vec{B}}|\psi_\alpha\rangle + c_{\alpha,\beta}\langle\psi_\alpha|\hat{\vec{B}}|\psi_\beta\rangle) - 1 \\ &= \frac{\langle r_n^2\rangle\mu_I}{IJA_p}\sum_\beta 2\,\mathrm{Re}(c_{\alpha,\beta}\langle\psi_\alpha|\hat{\vec{B}}|\psi_\beta\rangle), \end{aligned} \tag{3.21}$$

where the restriction on the summation index β is the same as in equation 3.20.

It is then expected that the variation in the hfs constant is approximately proportional to the variation in the mean squared radius of the nuclear charge distribution. The BR effect is therefore expected to be nearly proportional

to the difference in the mean squared radius of the charge distributions for the two isotopes, similarly to the case for the isotope shift in section 3.1.1. A linear fit on the form $C\delta\langle r_n^2\rangle$ can therefore be used to approximate the BR effect where the constant C can be determined with the MCDHF method for different charge distributions.

Chapter 4

Multi-Configuration Dirac-Hartree-Fock Method

The software package General Relativistic Atomic Structure Package 2018 (GRASP2018)[7] contains applications for calculations of electronic wave functions in atomic systems with the MCDHF method as well as calculations of different atomic properties such as the hfs constant.

4.1 Relativistic Atomic Physics

The Dirac-Coulomb (DC) Hamiltonian operator is used to describe the atomic system in which the Dirac Hamiltonian gives the kinetic and rest energies of the electrons while the potential energy is accounted for in a semi-classical manner with the attractive Coulomb potential between the electrons and a static, spherically symmetric nuclear charge distribution, and the repulsive Coulomb potential between the electrons. For a system of N electrons the DC Hamiltonian takes the form

$$\hat{H}_{DC} = \sum_{i=1}^{N}[c\vec{\alpha}_i \cdot \hat{\vec{p}}_i + (\beta - I_4)_i c^2 + \hat{V}_n(r_i)] + \sum_{i=1}^{N}\sum_{j>i}\frac{1}{r_{ij}}.$$

Here α_{ki} and β_i are the 4×4 Dirac matrices $\left[\begin{smallmatrix} 0 & \sigma_k \\ \sigma_k & 0 \end{smallmatrix}\right]_i$ and $\left[\begin{smallmatrix} I_2 & 0 \\ 0 & -I_2 \end{smallmatrix}\right]_i$ operating on the subspace of electron i. $\hat{\vec{p}}_i$ is the momentum operator for electron i. $\hat{V}_n(r_i)$ is the potential from a spherically symmetric nuclear charge distribution,

where r_i is the distance from the nuclear center to electron i. $r_{ij} = |\vec{r}_i - \vec{r}_j|$ is the distance between electrons i and j. c is the speed of light. The rest energy for each electron has been subtracted from the original Dirac Hamiltonian.

An approximation to the DC Hamiltonian can be made by assuming that the potential energy from the interactions between the electrons can be approximated with a spherically symmetric potential that for each electron is the average of the potential in the presence of the other electrons. This is known as the central field (CF) approximation and the approximate Hamiltonian becomes

$$\hat{H}_{CF} = \sum_{i=1}^{N} c\vec{\alpha}_i \cdot \hat{\vec{p}}_i + (\beta - I_4)_i c^2 + \hat{V}_i(r_i).$$

The CF Hamiltonian is a sum over operators where each term acts on the subspace of one electron only. Therefore the eigenvalue equation

$$\hat{H}_{CF}|\boldsymbol{\psi}\rangle = E|\boldsymbol{\psi}\rangle$$

has solutions that can be constructed as direct products of solutions to the one electron eigenvalue equations

$$[c\vec{\alpha}_i \cdot \hat{\vec{p}}_i + (\beta - I_4)_i c^2 + \hat{V}_i(r_i)]|\boldsymbol{\psi}_i\rangle = E_i|\boldsymbol{\psi}_i\rangle \tag{4.1}$$

with eigenvalues $E = \sum_{i=1}^{N} E_i$ since

$$\hat{H}_{CF}|\boldsymbol{\psi}_1\rangle \ldots |\boldsymbol{\psi}_N\rangle = \sum_{i=1}^{N} E_i|\boldsymbol{\psi}_1\rangle \ldots |\boldsymbol{\psi}_N\rangle = E|\boldsymbol{\psi}_1\rangle \ldots |\boldsymbol{\psi}_N\rangle.$$

Using spherical coordinates, the kinetic energy term $c\vec{\alpha}\cdot\hat{\vec{p}}$ can be expressed as [20, p. 136]

$$c\vec{\alpha} \cdot \hat{\vec{p}} = -ic\sigma_r(\partial_r + \frac{\hat{K}+1}{r}),$$

where $\sigma_r = \vec{\sigma} \cdot \vec{e}_r$ and $\vec{e}_r$ is the radial unit vector. The eigenfunctions of the operator $\hat{K} = -(1 + \vec{\sigma} \cdot \hat{\vec{l}})$ are the spherical spinors $\boldsymbol{\chi}_\kappa^m$ with corresponding

eigenvalues κ. The spherical spinors are coupled direct products of Pauli spinors and spherical harmonics. They are therefore also eigenfunctions of the squared angular momentum operators $\hat{\vec{j}}^2$, $\hat{\vec{l}}^2$, $\hat{\vec{s}}^2$ and the projection operator $\hat{j}_z$ where $\hat{\vec{j}} = \hat{\vec{l}} + \hat{\vec{s}}$. The corresponding eigenvalues are $j(j+1)$, $l(l+1)$, $s(s+1)$ and m where $j \in \{1/2, 3/2, \ldots\}$, $l \in \{0, 1, \ldots\}$, $s = 1/2$ and $m \in \{-j, -j+1, \ldots, j\}$. Since $\hat{\vec{\sigma}} \cdot \hat{\vec{l}} = 2\hat{\vec{l}} \cdot \hat{\vec{s}}$ the eigenvalues κ are given by

$$\begin{aligned}\kappa &= -(1 + j(j+1) - l(l+1) - \frac{3}{4}) = -j(j+1) + l(l+1) - \frac{1}{4} \\ &= \begin{cases} -(j + \frac{1}{2}) & \text{for } j = l + \frac{1}{2} \\ (j + \frac{1}{2}) & \text{for } j = l - \frac{1}{2} \end{cases}. \end{aligned} \tag{4.2}$$

Both the operators $\hat{K}$ and $\hat{j}_z$ are Hermitian and so the spherical spinors must satisfy the orthonormality condition $\langle \boldsymbol{\chi}_\kappa^m | \boldsymbol{\chi}_{\kappa'}^{m'} \rangle = \delta_{\kappa,\kappa'} \delta_{m,m'}$ for proper normalization factors.

Using the properties of the spherical spinors and that $\sigma_r | \boldsymbol{\chi}_\kappa^m \rangle = -| \boldsymbol{\chi}_{-\kappa}^m \rangle$ [20, p. 135], the one-electron wave functions on the form

$$\boldsymbol{\psi}_{n\kappa}^m(r_i, \theta_i, \phi_i) = [\frac{P_{n\kappa}(r_i)}{r_i} \boldsymbol{\chi}_\kappa^m(\theta_i, \phi_i), \frac{Q_{n\kappa}(r_i)}{r_i} \boldsymbol{\chi}_{-\kappa}^m(\theta_i, \phi_i)]^T \tag{4.3}$$

will solve equation 4.1 if the radial factors solve the resulting pair of radial equations

$$\hat{V}_i(r_i) P_{n\kappa}(r_i) - c(\partial_{r_i} - \frac{\kappa}{r_i}) Q_{n\kappa}(r_i) = E_{n\kappa} P_{n\kappa}(r_i) \tag{4.3a}$$

$$c(\partial_{r_i} + \frac{\kappa}{r_i}) P_{n\kappa}(r_i) + (\hat{V}_i(r_i) - 2c^2) Q_{n\kappa}(r_i) = E_{n\kappa} Q_{n\kappa}(r_i) \tag{4.3b}$$

since the spherical spinors factor out. The functions $P_{n\kappa}(r_i)$ and $Q_{n\kappa}(r_i)$ are known as the large and small components, respectively, since in the non-relativistic limit $Q_{n\kappa}(r_i)/P_{n\kappa}(r_i) \approx p/2c$, where p is the momentum of the electron.

In the case where the interactions between the electrons are neglected, the pair of equations reduces to the one for the hydrogen-like ion for which the possible radial functions for each value of κ are labeled by the principal

quantum number n. In the CF approximation the potential function can be viewed as a hydrogenlike potential with a screening parameter that varies along the radial axis and the solutions can be viewed as hydrogenic solutions that are scaled along the radial axis according to the screening and so the same labeling of the possible solutions can be used where the radial functions have the same number of nodes as in the hydrogenic case.

Each energy level $E_{n\kappa}$ is $(2j+1)$-fold degenerate due to the possible values of the quantum number m. Each label $\{n\kappa\}$ gives rise to a so-called subshell that contains $2j+1$ electron orbitals, one for each value of m. Since the electrons within the same subshell have the same energy they are sometimes called equivalent electrons. The pair of angular momentum quantum numbers $j = l \pm 1/2$ gives rise to two distinct subshells in the relativistic formulation which are combined to a single subshell labeled by the orbital quantum number l in the non-relativistic formulation. The non-relativistic notation for describing the electronic configuration of an atom is through the quantum numbers $n_{(i)}l_{(i)}$ for the subshells as well as the number of electrons $w_{(i)}$ in the subshell and takes the form

$$n_{(1)}l_{(1)}^{w_{(1)}}n_{(2)}l_{(2)}^{w_{(2)}}\ldots.$$

In the relativistic notation all the subshells with $l \neq 0$ are split up as

$$nl_{l-1/2}^{w^-}nl_{l+1/2}^{w^+},$$

where w^- and w^+ are the number of electrons in the corresponding relativistic subshells. For subshells with $l = 0$ the relativistic notation is $ns_{1/2}^{w}$.

For each subshell i the principal quantum number $n_{(i)}$ is labeled by a positive integer and the orbital quantum number $l_{(i)}$ is labeled by the letters $s, p, d, \ldots$. For subshells with one electron the number $w_{(i)} = 1$ is omitted. All filled subshells are usually also omitted in the notation.

The electron configuration of an atomic system is often described with the non-relativistic notation even if the relativistic theory is used. Which of the relativistic subshells that are involved then depends on the total angular momentum of the state.

4.2 Configuration State Functions

The wave function for a system of electrons should be antisymmetric w.r.t. the interchange of any two electron coordinates [8, p. 100]. A wave function that solves the eigenvalue equation and is antisymmetric w.r.t. coordinate interchanges can be constructed by the use of the antisymmetrization operator $\hat{A}$ on the direct product of one-electron wave functions. This is given by

$$\begin{aligned}\phi(\vec{x}_1, \ldots, \vec{x}_N; \boldsymbol{\gamma}) &= \hat{A}[\boldsymbol{\psi}_1(\vec{x}_1) \ldots \boldsymbol{\psi}_N(\vec{x}_N)] \\ &= \frac{1}{\sqrt{N!}} \sum_{P \in S_N} \mathrm{sgn}(P) \boldsymbol{\psi}_{P(1)}(\vec{x}_1) \ldots \boldsymbol{\psi}_{P(N)}(\vec{x}_N). \end{aligned} \quad (4.4)$$

Here S_N is the set of possible permutations of N objects. $P(i)$ is the index at position i of the permutation P. $\mathrm{sgn}(P)$ is the sign of the particular permutation which is positive for even permutations and negative for odd permutations from the original ordering with ascending indices $1, 2, \ldots, N$ in some chosen ordering convention for the one-electron wave functions. $\boldsymbol{\gamma}$ represents the quantum numbers needed to describe each of the one-electron wave functions. For the antisymmetric product function to be non-zero, all the one-electron wave functions used must be distinct, so the Pauli exclusion principle is fulfilled.

The total electronic system is not subjected to any external torque. Classically, this corresponds to the total angular momentum of the system being conserved. In the quantum mechanical picture, the wave function describing an electronic configuration state should be an eigenfunction of the squared and projection total angular momentum operators $\hat{\vec{J}}^2$ and $\hat{J}_z$ with eigenvalues $J(J+1)$ and M_J, respectively, with $J \in \{0, 1/2, 1, \ldots\}$ and $M_J \in \{-J, -J+1, \ldots, J\}$. The so-called configuration state functions (CSF) are constructed by angular momentum coupling of the antisymmetric wave functions with the same sets of quantum numbers $\{n\kappa\}$ through the CG-expansion. The angular momenta of the electrons can be coupled successively in the so-called jj-coupling scheme [8, p. 125] to give the CSFs

$$\Phi(\vec{x}_1, \ldots, \vec{x}_N; \boldsymbol{\alpha}, J^\pi, M_J) = \sum_{m_1, \ldots, m_N} C^{J, M_J}_{m_1, \ldots, m_N} \phi(\vec{x}_1, \ldots, \vec{x}_N; \boldsymbol{\gamma}(\boldsymbol{\alpha}; m_1, \ldots, m_N)), \quad (4.5)$$

where the product of CG-coefficients have been abbreviated with the factor $C^{J,M_J}_{m_1,\ldots,m_N}$. $\boldsymbol{\alpha}$ represents the quantum numbers needed to describe the CSF in addition to J and M_J, such as the principal and angular momentum quantum numbers of the subshells, and the coupling scheme used. $\boldsymbol{\gamma}(\boldsymbol{\alpha}; m_1, \ldots, m_N)$ represents the antisymmetrized direct product wave functions determined by the quantum numbers contained in $\boldsymbol{\alpha}$ and the particular set of magnetic quantum numbers $\{m_1, \ldots, m_N\}$. π represents the parity of the CSF which is given by the product of parity values of the constituent one-electron wave functions and can have the values ± 1. Since $\boldsymbol{\alpha}$ contains information about the one-electron wave functions, it also contains information about the total parity. However, the parity is sometimes given explicitly in the notation since this can be an important property to consider.

In many cases the different electronic subshells are considered as separate systems for which temporary wave functions for each subshell are constructed. The wave function of the total system is then formed from the temporary wave functions where only permutations of electron coordinates between different subshells are allowed and where the resultant angular momentum of each subshell are coupled [6, p. 24]. The total angular momentum of a filled subshell is always 0 and so it factors out of the coupling procedure [8, p. 107]. Since many applications in atomic systems involve several filled subshells, this method makes the coupling procedure relatively simple.

In the relativistic formulation, the spin and orbital angular momentum of each electron are coupled intrinsically in the one-electron wave functions. The total angular momenta j of each electron are then coupled together, known as jj-coupling. In non-relativistic quantum mechanics, the spin properties are added in a more ad hoc fashion where the wave functions are constructed from direct products of solutions to the Schrödinger equation and Pauli spinors. The spin and orbital angular momenta are then usually coupled separately to total orbital angular momentum L and total spin S which in turn can be coupled to total angular momentum J, known as LS-coupling. In non-relativistic quantum mechanics the spin and orbital angular momenta do not interact with each other intrinsically so both L and S are considered good quantum numbers unless explicit coupling interactions are introduced.

It is customary to describe the possible angular momentum states associated with a given electron configuration in the so-called LS-notation ${}^{(2S+1)}L_J$ where only J is a good quantum number in the relativistic formulation. The angular momentum eigenstates with a given value of J can then generally be a linear combination of states with equal value of J but with different

values of L and S. The term ${}^{(2S+1)}L_J$ is then used to refer to the eigenstate in which ${}^{(2S+1)}L_J$ is the dominant component.

The possible CSFs for an electronic system are orthonormal as long as the one-electron wave functions are orthonormal since

$$\begin{aligned}
&\langle \boldsymbol{\alpha}; J^{\pi}, M_J | \boldsymbol{\alpha}'; J'^{\pi'}, M'_J \rangle \\
&= \sum_{\substack{m_1..m_N \\ m'_1..m'_N}} C^{J,M_J}_{m_1..m_N} C^{J',M'_J}_{m'_1..m'_N} \frac{1}{N!} \sum_{PP'} \mathrm{sgn}(P)\mathrm{sgn}(P') \langle \boldsymbol{\psi}_{P(1)} | \boldsymbol{\psi}_{P'(1)} \rangle .. \langle \boldsymbol{\psi}_{P(N)} | \boldsymbol{\psi}_{P'(N)} \rangle \\
&= \sum_{\substack{m_1..m_N \\ m'_1..m'_N}} C^{J,M_J}_{m_1..m_N} C^{J',M'_J}_{m'_1..m'_N} \frac{1}{N!} \sum_{PP'} \mathrm{sgn}(P)\mathrm{sgn}(P') \delta_{P,P'} \delta_{m_1,m'_1} .. \delta_{m_N,m'_N} \delta_{\boldsymbol{\alpha},\boldsymbol{\alpha}'} \\
&= \sum_{m_1..m_N} C^{J,M_J}_{m_1..m_N} C^{J',M'_J}_{m_1..m_N} \frac{1}{N!} N! \delta_{\boldsymbol{\alpha},\boldsymbol{\alpha}'} = \delta_{\boldsymbol{\alpha},\boldsymbol{\alpha}'} \delta_{J,J'} \delta_{M_J,M'_J}. \qquad (4.6)
\end{aligned}$$

In the third line it has been used that the one-electron wave functions in each inner product must be identical for the total product to be non-zero. In the last line the orthonormality of the CG-coefficients has been used successively.

4.2.1 Example: $1s2p\ {}^3P_1$ in He

In the CF approximation, the state $1s2p\ {}^3P_1$ in He is a linear combination of the relativistic configurations $1s_{1/2}2p_{1/2}$ and $1s_{1/2}2p_{3/2}$ with $J = 1$. The coordinate system can be chosen so that $M_J = J = 1$. The parity is $\pi = -1$.

The CSF for $1s_{1/2}2p_{1/2}$ is constructed from the one-electron wave functions $\boldsymbol{\psi}^{m_1}_{1,-1}$ and $\boldsymbol{\psi}^{m_2}_{2,1}$, where the notation with n, κ and m from equation 4.3 is used. Antisymmetrization of the direct product functions becomes

$$\phi(\vec{x}_1, \vec{x}_2; 1s_{1/2}2p_{1/2}, m_1, m_2) = \frac{1}{\sqrt{2}} [\boldsymbol{\psi}^{m_1}_{1,-1}(\vec{x}_1) \boldsymbol{\psi}^{m_2}_{2,1}(\vec{x}_2) - \boldsymbol{\psi}^{m_2}_{2,1}(\vec{x}_1) \boldsymbol{\psi}^{m_1}_{1,-1}(\vec{x}_2)], \qquad (4.7)$$

where $\vec{x}_1$ and $\vec{x}_2$ are the coordinates of the two electrons. The labeling of the electrons is in principle arbitrary, but the resulting functions will differ from each other by a phase factor of -1. The corresponding CSF becomes

$$
\begin{aligned}
&\Phi(\vec{x}_1, \vec{x}_2; 1s_{1/2}2p_{1/2}, 1^{-1}, 1) \\
&= \frac{1}{\sqrt{2}} \sum_{m_1,m_2} C^{1,1}_{m_1,m_2} [\boldsymbol{\psi}^{m_1}_{1,-1}(\vec{x}_1)\boldsymbol{\psi}^{m_2}_{2,1}(\vec{x}_2) - \boldsymbol{\psi}^{m_2}_{2,1}(\vec{x}_1)\boldsymbol{\psi}^{m_1}_{1,-1}(\vec{x}_2)] \\
&= \frac{1}{\sqrt{2}} [\boldsymbol{\psi}^{1/2}_{1,-1}(\vec{x}_1)\boldsymbol{\psi}^{1/2}_{2,1}(\vec{x}_2) - \boldsymbol{\psi}^{1/2}_{2,1}(\vec{x}_1)\boldsymbol{\psi}^{1/2}_{1,-1}(\vec{x}_2)], \qquad (4.8)
\end{aligned}
$$

since the only non-zero CG coefficient is $C^{1,1}_{1/2,1/2} = 1$.

Correspondingly, the CSF for the configuration $1s_{1/2}2p_{3/2}$ is constructed from the one-electron functions $\boldsymbol{\psi}^{m_1}_{1,-1}$ and $\boldsymbol{\psi}^{m_2}_{2,-2}$ where the antisymmetrized direct product is

$$
\phi(\vec{x}_1, \vec{x}_2; 1s_{1/2}2p_{3/2}, m_1, m_2) = \frac{1}{\sqrt{2}} [\boldsymbol{\psi}^{m_1}_{1,-1}(\vec{x}_1)\boldsymbol{\psi}^{m_2}_{2,-2}(\vec{x}_2) - \boldsymbol{\psi}^{m_2}_{2,-2}(\vec{x}_1)\boldsymbol{\psi}^{m_1}_{1,-1}(\vec{x}_2)]. \qquad (4.9)
$$

The CSF then becomes

$$
\begin{aligned}
&\Phi(\vec{x}_1, \vec{x}_2; 1s_{1/2}2p_{3/2}, 1^{-1}, 1) \\
&= \frac{1}{\sqrt{2}} \sum_{m_1,m_2} C^{1,1}_{m_1,m_2} [\boldsymbol{\psi}^{m_1}_{1,-1}(\vec{x}_1)\boldsymbol{\psi}^{m_2}_{2,-2}(\vec{x}_2) - \boldsymbol{\psi}^{m_2}_{2,-2}(\vec{x}_1)\boldsymbol{\psi}^{m_1}_{1,-1}(\vec{x}_2)] \\
&= -\frac{1}{2\sqrt{2}} [\boldsymbol{\psi}^{1/2}_{1,-1}(\vec{x}_1)\boldsymbol{\psi}^{1/2}_{2,-2}(\vec{x}_2) - \boldsymbol{\psi}^{1/2}_{2,-2}(\vec{x}_1)\boldsymbol{\psi}^{1/2}_{1,-1}(\vec{x}_2)] \\
&\quad + \frac{\sqrt{3}}{2\sqrt{2}} [\boldsymbol{\psi}^{-1/2}_{1,-1}(\vec{x}_1)\boldsymbol{\psi}^{3/2}_{2,-2}(\vec{x}_2) - \boldsymbol{\psi}^{3/2}_{2,-2}(\vec{x}_1)\boldsymbol{\psi}^{-1/2}_{1,-1}(\vec{x}_2)]. \qquad (4.10)
\end{aligned}
$$

For this CSF there are two non-zero CG coefficients, $C^{1,1}_{1/2,1/2} = -1/2$ and $C^{1,1}_{-1/2,3/2} = \sqrt{3}/2$.

4.3 Configuration Interaction

The CSFs can sometimes be good approximations to the eigenfunctions of the DC Hamiltonian [6, p. 13]. However, better approximations can be made by use of the method of configuration interaction (CI).

Since the distinct one-electron wave functions form a complete basis for functions in the one-electron Hilbert space, the set of all CSFs that can be

formed from these one-electron wave functions will form a basis for all possible functions in the Hilbert space for the entire electronic system that also are antisymmetric w.r.t. interchanges of pairs of electron coordinates. Any bound eigenstate of the DC Hamiltonian could then technically be expressed as a linear combination of eigenstates of the CF Hamiltonian. Generally this would require an infinite number of CSFs, but a good estimate can often be formed with a finite number when the most significant CSFs are used.

When there is no external torque exerted on the electronic system the eigenfunctions of the DC Hamiltonian must also be eigenfunctions of the parity and total angular momentum operators. The set of CSFs in which these eigenfunctions can be expanded can therefore be restricted to CSFs with the same total angular momentum quantum numbers and parity.

Assuming that the difference between the DC and CF Hamiltonians is relatively small compared with the atomic energies, an estimate for the contributions from the various CSFs to a given configuration can be made using first order perturbation theory with the perturbing operator [10, p. 13]

$$\hat{h} = \hat{H}_{DC} - \hat{H}_{CF} = \sum_{i=1}^{N} [\sum_{j>i} \frac{1}{r_{ij}} - \hat{V}_i(r_i)]. \tag{4.11}$$

The energy levels of the CSFs are $(2J+1)$-fold degenerate but since the CSF expansion is restricted to a single value of M_J the non-degenerate method can be used. The first order correction to the CSF $|\boldsymbol{\alpha}; J^\pi, M_J\rangle$ is then

$$|\boldsymbol{\alpha}; J^\pi, M_J\rangle^{(1)} = \sum_{\boldsymbol{\beta} \neq \boldsymbol{\alpha}} |\boldsymbol{\beta}; J^\pi, M_J\rangle \frac{\langle \boldsymbol{\beta}; J^\pi, M_J | \hat{h} | \boldsymbol{\alpha}; J^\pi, M_J \rangle}{E_{\boldsymbol{\alpha}} - E_{\boldsymbol{\beta}}}, \tag{4.12}$$

where the sum over $\boldsymbol{\beta}$ can be restricted to the CSFs that differ by maximally two electron orbitals from $|\boldsymbol{\alpha}; J^\pi, M_J\rangle$ since $\hat{h}$ is a two-electron operator. The denominator in these expansion coefficients indicates that the larger the energy difference is between the CSF to be corrected and any other CSF contributing to the correction, the smaller its contribution is expected to be. Also the contribution from a particular CSF depends on the positional correlation between the electrons. The numerator $\langle \boldsymbol{\beta}; J^\pi, M_J | \hat{h} | \boldsymbol{\alpha}; J^\pi, M_J \rangle$ is a measure of the tendency for the CSFs to cause each other to deviate energetically from the CF approximation.

The approximations to the eigenfunctions of the DC Hamiltonian that are formed from expansions of CSFs are known as atomic state functions (ASF). With *NCF* being the number of CSFs included in the expansion, the expression for the ASF becomes

$$\Psi(\vec{x}_1, \ldots, \vec{x}_N; J^\pi, M_J) = \sum_{i=1}^{NCF} c_i \Phi(\vec{x}_1, \ldots, \vec{x}_N; \boldsymbol{\alpha}_i, J^\pi, M_J), \tag{4.13}$$

where the expansion coefficients c_i can be determined from the energies associated with interactions between the CSFs.

4.4 The Variational Method

The energy functional $\mathcal{E}$ of a state $|\Psi\rangle$ is defined as [6, p. 14]

$$\mathcal{E} \equiv \frac{\langle \Psi | \hat{H} | \Psi \rangle}{\langle \Psi | \Psi \rangle}. \tag{4.14}$$

Under arbitrary infinitesimal changes $|\delta\Psi\rangle$ to the state vector there will generally be infinitesimal changes $\delta\mathcal{E}$ and $\delta\hat{H}$ to the energy functional and Hamiltonian operator, respectively. These are related by

$$\delta\mathcal{E}\langle\Psi|\Psi\rangle + \mathcal{E}(\langle\delta\Psi|\Psi\rangle + \langle\Psi|\delta\Psi\rangle) = \langle\delta\Psi|\hat{H}|\Psi\rangle + \langle\Psi|\hat{H}|\delta\Psi\rangle + \langle\Psi|\delta\hat{H}|\Psi\rangle. \tag{4.15}$$

Since $\langle\Psi|\Psi\rangle = 1$ from normalization of the state vector and $\langle\Psi|\hat{H}|\delta\Psi\rangle = \langle\delta\Psi|\hat{H}|\Psi\rangle^*$ from Hermicity of the Hamiltonian this can be expressed as

$$\delta\mathcal{E} - \langle\Psi|\delta\hat{H}|\Psi\rangle = 2\mathrm{Re}(\langle\delta\Psi|(\hat{H} - \mathcal{E})|\Psi\rangle). \tag{4.16}$$

If the Hamiltonian is stationary to first order under the changes in the state vector, the condition $\delta\mathcal{E} = 0$ implies

$$\hat{H}|\Psi\rangle = \mathcal{E}|\Psi\rangle, \tag{4.17}$$

which means that the state is an eigenstate of the Hamiltonian.

In order to keep the wave functions orthonormal, Lagrange multipliers are introduced to enforce the constraints that the radial functions $\boldsymbol{R}_a \equiv [P_a, iQ_a]^T$ should be normalized and orthogonal to all other radial functions

with the same quantum number κ, and that the expansion coefficients in the ASF are such that the ASF remains normalized. This gives the variational functional

$$\mathcal{F} = \mathcal{E} + \sum_{a,b} \delta_{\kappa_a,\kappa_b} \lambda_{a,b} \langle \boldsymbol{R}_a | \boldsymbol{R}_b \rangle + \Lambda \sum_i |c_i|^2. \tag{4.18}$$

The condition $\delta\mathcal{F} = 0$ under variations in the radial functions and expansion coefficients in a particular ASF is used to obtain the multi-configuration Dirac-Hartree-Fock equations.

The energy functional for an ASF that is kept normalized can be expressed as

$$\mathcal{E}_{ASF} = \langle \Psi | \hat{H}_{DC} | \Psi \rangle = \sum_{k,n} c_k c_n \langle \Phi(\boldsymbol{\alpha}_k) | \hat{H}_{DC} | \Phi(\boldsymbol{\alpha}_n) \rangle. \tag{4.19}$$

4.4.1 Calculation of Radial Functions

The DC Hamiltonian can be expressed as a sum over one-electron operators $\hat{h}_i$ and two-electron operators $\hat{h}_{ij}$. The matrix elements in equation 4.19 are therefore composed of one-electron and two-electron matrix elements. The one-electron elements take the form

$$\begin{aligned} &\langle \boldsymbol{\psi}_a^{m_a} | \hat{h}_i | \boldsymbol{\psi}_b^{m_b} \rangle = \delta_{\kappa_a,\kappa_b} \delta_{m_a,m_b} \\ &\times \int_0^\infty dr_i [P_a(r_i), -iQ_a(r_i)] \begin{bmatrix} V_n(r_i) & ic(\partial_{r_i} - \kappa_b/r_i) \\ ic(\partial_{r_i} + \kappa_b/r_i) & V_n(r_i) - 2c^2 \end{bmatrix} [P_b(r_i), iQ_b(r_i)]^T \end{aligned} \tag{4.20}$$

where the labels a and b refer to subshells in the CSFs $\Phi(\boldsymbol{\alpha}_k)$ and $\Phi(\boldsymbol{\alpha}_n)$ respectively. The two-electron elements take the form

$$\langle \boldsymbol{\psi}_a^{m_a} | \langle \boldsymbol{\psi}_b^{m_b} | \hat{h}_{ij} | \boldsymbol{\psi}_d^{m_d} \rangle | \boldsymbol{\psi}_c^{m_c} \rangle = \int d\vec{r}_i d\vec{r}_j [P_a(r_i) P_c(r_i) \boldsymbol{\Omega}_{\kappa_a}^{m_a\dagger}(\theta_i, \phi_i) \boldsymbol{\Omega}_{\kappa_c}^{m_c}(\theta_i, \phi_i)$$
$$+ Q_a(r_i) Q_c(r_i) \boldsymbol{\Omega}_{-\kappa_a}^{m_a\dagger}(\theta_i, \phi_i) \boldsymbol{\Omega}_{-\kappa_c}^{m_c}(\theta_i, \phi_i)] [P_b(r_j) P_d(r_j) \boldsymbol{\Omega}_{\kappa_b}^{m_b\dagger}(\theta_j, \phi_j) \boldsymbol{\Omega}_{\kappa_d}^{m_d}(\theta_j, \phi_j)$$
$$+ Q_b(r_j) Q_d(r_j) \boldsymbol{\Omega}_{-\kappa_b}^{m_b\dagger}(\theta_j, \phi_j) \boldsymbol{\Omega}_{-\kappa_d}^{m_d}(\theta_j, \phi_j)] \sum_{l=0}^{\infty} \frac{r_<^l}{r_>^{l+1}} P_l(\cos\omega)$$
$$= \sum_{l=0}^{\infty} \int dr_i dr_j \frac{r_<^l}{r_>^{l+1}} [{}^l f_{ac,bd}^{m_a,m_c,m_b,m_d} P_a(r_i) P_c(r_i) P_b(r_j) P_d(r_j)$$
$$+ {}^l f_{ac,-bd}^{m_a,m_c,m_b,m_d} P_a(r_i) P_c(r_i) Q_b(r_j) Q_d(r_j) + {}^l f_{-ac,bd}^{m_a,m_c,m_b,m_d} Q_a(r_i) Q_c(r_i) P_b(r_j) P_d(r_j)$$
$$+ {}^l f_{-ac,-bd}^{m_a,m_c,m_b,m_d} Q_a(r_i) Q_c(r_i) Q_b(r_j) Q_d(r_j)], \tag{4.21}$$

where the labels a and b refer to subshells in $\Phi(\boldsymbol{\alpha}_k)$, and c and d to subshells in $\Phi(\boldsymbol{\alpha}_n)$. Here the Laplace expansion in terms of Legendre polynomials [6, p. 30]

$$\frac{1}{|\vec{r}_i - \vec{r}_j|} = \sum_{l=0}^{\infty} \frac{r_<^l}{r_>^{l+1}} P_l(\cos\omega) \tag{4.22}$$

has been used in order to separate the radial and angular integrals. $r_<$ and $r_>$ are respectively the lesser and greater of $r_i = |\vec{r}_i|$ and $r_j = |\vec{r}_j|$. ω is the angle between $\vec{r}_i$ and $\vec{r}_j$, and $P_l(x)$ is the Legendre polynomial of degree l. Since the angular parts of the one-electron wave functions are known to be the spherical spinors, the angular integrals have been compressed into prefactors which are constant through optimization of the radial functions. Although the sum is over an infinite number of l-values, only a finite number of them give non-zero prefactors since they ultimately can be decomposed into integrals over products of three spherical harmonics. From the properties of the spherical harmonics [8, p. 146], this puts a limit on l not to exceed $2\max(l_a, l_b, l_c, l_d)$ where l_a is the orbital quantum number of orbital a etc.

Due to the inner products of all the other one-electron wave functions which are multiplied with each of the one- and two-electron matrix elements, only CSFs that differ by maximally two electron orbitals can have a non-zero matrix element in equation 4.19.

Since the total energy functional is a linear combination of the one- and two-electron matrix elements, the variation $\delta\mathcal{F}$ can be expressed as the linear combination of variations in these terms resulting from arbitrary small

variations δP_k and δQ_k for each subshell k included in the ASF. The condition $\delta\mathcal{F} = 0$ leads to a set of integro-differential equations for all pairs of radial functions P_k and Q_k given some initial estimates of the functions and the ASF expansion coefficients. The radial functions should also satisfy the boundary conditions

$$\lim_{r\to 0} P_k(r) = \lim_{r\to\infty} P_k(r) = \lim_{r\to 0} Q_k(r) = \lim_{r\to\infty} Q_k(r) = 0 \tag{4.23}$$

Due to the configuration mixing, the matrix elements between different CSFs introduce some degree of coupling between the radial equations for the orbitals that are different between the CSFs. With the use of a numerical scheme, the equations can be solved to get better approximations for the radial functions if the initial estimates are sufficiently accurate.

4.4.2 Calculation of Expansion Coefficients

Assuming the CSFs to be known, and organizing the expansion coefficients in a vector $\boldsymbol{c}$ and the matrix elements from equation 4.19 in a matrix H, variations $\delta\mathcal{F}$ resulting from arbitrary infinitesimal variations $\delta\boldsymbol{c}$ can be expressed as

$$(\delta\boldsymbol{c})^\dagger H\boldsymbol{c} + \boldsymbol{c}^\dagger H(\delta\boldsymbol{c}) + \Lambda((\delta\boldsymbol{c})^\dagger\boldsymbol{c} + \boldsymbol{c}^\dagger(\delta\boldsymbol{c})) = 2\mathrm{Re}(\delta\boldsymbol{c}^\dagger(H+\Lambda)\boldsymbol{c}).$$

The condition $\delta\mathcal{F} = 0$ leads to the eigenvalue equation

$$H\boldsymbol{c} = -\Lambda\boldsymbol{c} \tag{4.24}$$

for which the solutions $\boldsymbol{c}$ contain the sets of expansion coefficients for the possible ASFs that can be constructed from the particular set of CSFs, with corresponding ASF energy eigenvalues $-\Lambda$. The different ASFs can be seen as corrections to the CSF which is the largest component in the ASF.

The radial functions and expansion coefficients are optimized in an iterative procedure where the integro-differential equations for each set of radial functions are solved with previous estimates of the functions themselves and the expansion coefficients. With the newly obtained radial functions, equation 4.24 is solved to obtain new estimates for the expansion coefficients before the process is repeated with the new radial functions and expansion

coefficients as initial estimates. When the difference between the estimated wave function and a true eigenfunction of the DC Hamiltonian is small, the change in the Hamiltonian becomes small since it is stationary to first order for the true eigenfunctions. The change of the radial functions will then also be small. The procedure is repeated until the change in the wave function from the previous estimate is less than a threshold tolerance. The solution is then said to have reached self consistency.

More details on the theory used for the MCDHF method in GRASP2018 has been presented Dyall et al. [9].

4.4.3 Example: $1s2p\ ^3P_1$ in He

Continuing the example with the state $1s2p\ ^3P_1$, the ASF can in a first approximation be formed with the minimal expansion with the CSFs $\Phi(\vec{x}_1, \vec{x}_2; 1s_{1/2}2p_{1/2}, 1^{-1}, 1)$ and $\Phi(\vec{x}_1, \vec{x}_2; 1s_{1/2}2p_{3/2}, 1^{-1})$ as

$$\Psi(\vec{x}_1, \vec{x_2}; 1s2p^3P_1, 1^{-1}, 1) = \tag{4.25}$$
$$c_{1s_{1/2}2p_{1/2}}\Phi(\vec{x}_1, \vec{x_2}; 1s_{1/2}2p_{1/2}, 1^{-1}, 1) + c_{1s_{1/2}2p_{3/2}}\Phi(\vec{x}_1, \vec{x_2}; 1s_{1/2}2p_{3/2}, 1^{-1}, 1).$$

The radial functions $[P_{1,-1}(r), iQ_{1,-1}(r)]^T$, $[P_{2,1}(r), iQ_{2,1}(r)]^T$ and $[P_{2,-2}(r), iQ_{2,-2}(r)]^T$ need to be determined along with expansion coefficients $c_{1s_{1/2}2p_{1/2}}$ and $c_{1s_{1/2}2p_{3/2}}$. Typically the number of CSFs included is much larger, but this example serves as an illustration of the method.

Using the MCDHF method with GRASP2018 the expansion coefficients were found to be $c_{1s_{1/2}2p_{1/2}} = 0.8166$ and $c_{1s_{1/2}2p_{3/2}} = -0.5773$. The radial functions are shown in Figure 4.1. The large component for the subshells $2p_{1/2}$ and $2p_{3/2}$ are nearly identical. This is expected since relativistic effects are small in light elements and the two functions are identical in the non-relativistic limit. The ratio between the amplitudes of the small and large components are approximately 0.007 which is close to the expected ratio in the non-relativistic limit $Q(r)/P(r) \approx Z\alpha/2 = \alpha \approx 0.0073$, where α is the fine structure constant. A static point charge was used for the nucleus in the calculations.

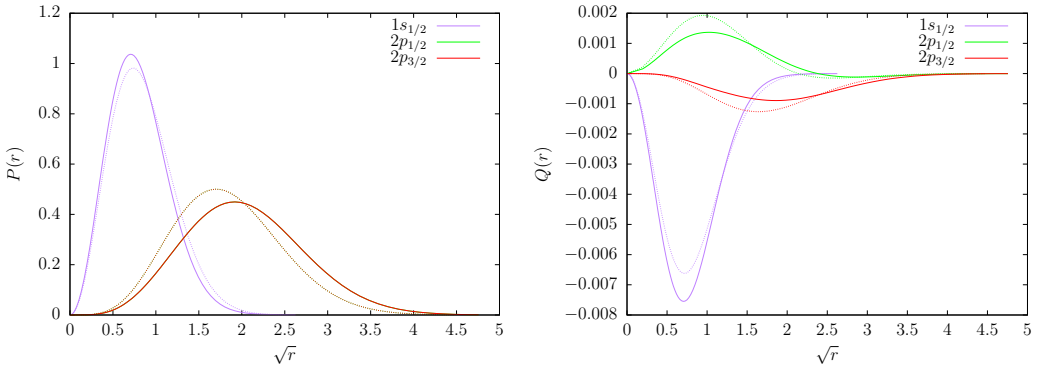

Figure 4.1: Large (left) and small (right) components of the radial functions for the subshells $1s_{1/2}$, $2p_{1/2}$ and $2p_{3/2}$ for the state $1s2p\ ^3P_1$ in He. The dotted lines are the initial estimates with the Thomas-Fermi approximation. The horizontal axis shows the square root of the radial distance which is measured in Bohr radii a_0.

4.5 Additional Corrections

Using fixed radial functions, the configuration interaction method can be used with the addition of further corrections to the Hamiltonian. The leading correction to the semi-classical Coulomb potential from the electron-electron interaction is the transverse photon correction [16, p. 34]

$$\hat{H}_T = -\sum_{i=1}^{N}\sum_{j>i}[\boldsymbol{\alpha}_i \cdot \boldsymbol{\alpha}_j \frac{\cos(\omega_{ij} r_{ij}/c)}{r_{ij}} + (\boldsymbol{\alpha}_i \cdot \nabla_j)(\boldsymbol{\alpha}_j \cdot \nabla_j)\frac{\cos(\omega_{ij} r_{ij}/c) - 1)}{\omega_{ij}^2 r_{ij}/c^2}], \tag{4.26}$$

where ω_{ij} is the frequency of the photon in the interaction between electrons i and j. In GRASP2018 this frequency is assumed to be given by the difference in orbital energies of the electrons [16, p. 35]. For multiply occupied orbitals and so-called virtual orbitals, this assumption may be too imprecise and a scale factor is often multiplied with the frequency. The scale factor is often set to 10^{-6}[16, p. 35]. With scaled frequencies this is also known as the Breit correction.

Corrections arising from quantum electrodynamics (QED) such as vacuum polarization and self energy can also be included. Vacuum polarization gives a correction to the Coulomb interactions due to polarization of virtual

electron-positron pairs. Self energy is the correction to the energy of each electron arising from interactions between the electron and virtual photons. In GRASP2018 the self energy is calculated with screened hydrogenic wave functions, which is only considered to be appropriate for the so-called spectroscopic orbitals [16, p. 35]. More on the theory behind these kinds of corrections has been presented by Schwerdtfeger et al. [22].

Chapter 5

Computations on ^{199}Hg

The spectroscopic states $^3P_1$ and $^3P_2$ of the electron configuration $6s6p$ are suitable for studying the BR effect in Hg. The stable isotope ^{199}Hg was chosen as a reference isotope for which values for the root-mean-square (rms) radius of the nuclear charge distribution has been obtained from experiments [12]. The nuclear angular momentum and magnetic moment were obtained from the IAEA Nuclear Data Section [14]. The hfs constants for the states $^3P_1$ and $^3P_2$ have been obtained experimentally from spectroscopic measurements [25],[19].

5.1 Nuclear Model

The finite charge distribution of the nucleus can be modeled in different ways with different degrees of complexity. One of the simplest models is a sphere with a homogeneous charge distribution. A model that has been used extensively is the two parameter Fermi distribution [5, p. 27] in equation 5.1 for which the homogeneous sphere is a limiting case when the parameter a approaches 0. Experiments with scattering of electrons has shown that nuclei do not have sharp edges [4, p. 87]. The Fermi distribution has the advantage over the homogeneous sphere that a discontinuous edge of the nucleus can be avoided. Other distribution functions can be used as well such as the modified Gaussian distribution [4, p. 91] or the three parameter Fermi distribution [4, p. 90]. The latter can be used to account for depressions or elevations of the charge distribution along the radial axis.

The use of a spherically symmetric charge distribution simplifies calcu-

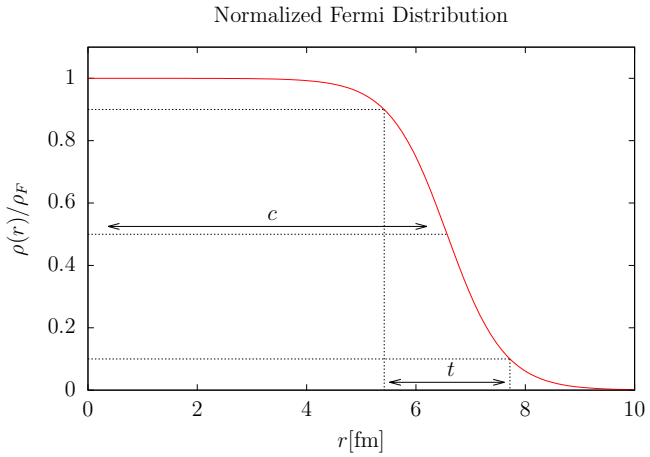

Figure 5.1: Fermi distribution with halfway radius c and skin thickness t for the nuclear model of ^{199}Hg.

lations of the electronic wave functions. Deformations of the nucleus can be accounted for by perturbative corrections using an electric quadrupole moment as in equation 3.2 if needed.

GRASP2018 allows for a two parameter Fermi distribution to be used to approximate the nuclear charge distribution which is given by the expression [5, p. 28]

$$\rho(r) = \frac{\rho_F}{1 + \exp\{(r - c)/a\}}. \tag{5.1}$$

The parameter c is the distance at which the value of the radial distribution has been reduced to 50 % of the value at the nuclear center. The parameter a is related to the so-called skin thickness t by $t = a \cdot 4 \ln 3$. The skin thickness is the radial distance over which the value of the radial distribution reduces from 90 % to 10 % of that at the nuclear center. The value of ρ_F is determined by the integral of the charge density over the entire space being equal to the nuclear charge Z, which gives $\rho_F = (3Z/4\pi c^2)(1 + \pi^2 a^2/c^2)^{-1}$ [5, p. 28]. Figure 5.1 shows the normalized Fermi distribution $\rho(r)/\rho_F$ for the nuclear model as defined by the values in Table 5.1.

For the computations on ^{199}Hg, the default skin thickness provided by GRASP2018 was used while the experimental value of the nuclear rms radius was provided to the program manually for it to calculate the corresponding value of the parameter c.

r_{rms} fm	t fm	I $\hbar$	μ_I μ_N
5.4474(31), [12]	2.3, [1]	1/2, [14]	0.5058855(9), [14]

Table 5.1: Values used to define the nuclear model for ^{199}Hg. r_{rms} is the rms nuclear charge radius, t is the nuclear skin thickness, I is the nuclear angular momentum and μ_I is the nuclear magnetic moment.

$A_{^3P_1}$ MHz	$A_{^3P_2}$ MHz
14752.37(1), [25]	9066.6236(20), [19]

Table 5.2: Experimental values of the hyperfine constant for the states $6s6p$ $^3P_1$ and $^3P_2$ in ^{199}Hg.

Further, the nucleus is modeled with a magnetic point dipole moment at the center for a perturbative calculation of the hfs constant where the zero-order wave function w.r.t. the hfs is obtained with the Fermi charge distribution.

The values used to define the nuclear model of the isotope ^{199}Hg are presented in Table 5.1. The experimentally measured values of the hfs constants for the states $^3P_1$ and $^3P_2$ are shown in Table 5.2.

According to Poisson's equation, the electric interaction between the Fermi nucleus, or a spherically symmetric charge distribution generally, and an electron is described by the potential [5, p. 10]

$$V_n(r) = -4\pi\big[\frac{1}{r}\int_0^r dr' r'^2 \rho(r') + \int_r^\infty dr' r' \rho(r')\big]. \tag{5.2}$$

5.2 Computation of Wave Functions

The process of calculating the wave function with GRASP2018 is divided into several steps. The first step is to define the CSF expansion for the ASF. The angular coefficients corresponding to the prefactors in equation 4.21 are then computed and stored for the subsequent self-consistent field (scf) calculations with the MCDHF method. Initial estimates of the radial functions are generated based on some simpler and less precise approximation such as

screened hydrogenic functions or Thomas-Fermi (TF) functions, which have the same qualitative characteristics as the functions that are sought for, such as the number of of nodes.

The solution is considered to be converged if the change between each iteration is smaller than a threshold. In GRASP2018 this change is based on a weighted sum over changes in the radial functions included in the ASF. A threshold parameter can be set for the program with which the weighted sum over changes is compared. The default threshold of 10^{-8} was used for the calculations in this project which is the same value as the one used for the calculations on ^{201}Hg [15].

After a solution to the scf calculations has been obtained, new ASF expansion coefficients are obtained with the transverse photon and QED corrections.

5.3 Generating the CSF Expansion for the ASF

The CSF expansions used for calculations of the electronic wave functions with GRASP2018 are generated with rules for substitutions of electron orbitals in one or several reference configurations with orbitals corresponding to excited electrons. The orbitals of the reference are called spectroscopic orbitals while the other orbitals used are called virtual orbitals. Virtual orbitals are sometimes referred to as correlation orbitals as they are used to capture energy deviations related to positional correlation between the electrons. The virtual orbitals, along with the subset of spectroscopic orbitals with which substitutions are made, are referred to as the active set (AS).

Sets of CSFs are often systematized by the amount of substitutions used to generate them from the reference, and further into whether the substitutions are made from valence orbitals or orbitals in closed subshells, called core orbitals.

The CSFs formed by single or double substitutions should capture the most significant parts of the ASF. The use of more than two substitutions would result in CSFs that have Hamiltonian matrix elements of zero with the CSF from which they were generated since the Hamiltonian operator consists of one- and two-electron operators. In that sense the CSFs other than those generated with single or double substitutions belong to higher

order corrections.

5.3.1 Single Substitutions

Since the point dipole hfs operator is a sum over one-electron operators, the CSFs generated by single substitutions are expected to capture a relatively large part of the hfs energy levels in a first approximation [6, p. 171]. Single substitutions from the electron core represent polarization of the originally closed subshells. The closed subshells produce zero net magnetic field at the nucleus, but when the subshells are polarized, the net magnetic field could become non-zero. Since the magnetic interaction between the nucleus and each electron are stronger with smaller distances, the core electrons could have a relatively large effect on the hfs value under polarization [6, p. 171]. This is especially the case for $s_{1/2}$ and $p_{1/2}$ subshells which have non-zero densities at the nucleus. Spin dependent polarization of these subshells can induce a difference in densities between spin directions which in turn results in contributions from the contact term in the hfs Hamiltonian [6, p. 171].

5.3.2 Double Substitutions

The CSFs generated from double substitutions are systematized into those generated from valence-valence (vv), core-valence (cv) and core-core (cc) substitutions and represent different correlation effects that are important for calculations of atomic properties [16, p. 42].

vv substitutions include those where both substitutions are made from valence orbitals. The energy differences between the valence orbitals and excited orbitals are relatively low and one might expect these substitutions to be important for improvement of the approximated wave function as this results in small denominators in the coefficients from the first order estimation in equation 4.12.

cv substitutions include those where one substitution is made from a core orbital and one from a valence orbital. These are also important for polarization of the core [6, p. 114] and cv substitutions from subshells deep in the core are important for calculations of the hfs constant [16, p. 42].

The cc substitutions include those where both substitutions are from core orbitals. If many core orbitals are open for cc substitutions the number of CSFs can increase dramatically.

5.4 Radial Grid

The radial functions are represented numerically by values on a radial grid. In GRASP2018 the distance from the atomic center to grid point number I is given by

$$R_I = RNT[\exp\{(I-1)H\} - 1], \quad I = 1, 2, 3, \ldots, NNNP, \tag{5.3}$$

where $RNT = 2.0 \cdot 10^{-6}$ and $H = 5.0 \cdot 10^{-2}$ by default. The smaller values $RNT = 1.0 \cdot 10^{-6}$ and $H = 1.0 \cdot 10^{-2}$ have been recommended for Hg in the older version of the program, GRASP2K [21]. In GRASP2018 the default value of RNT is further divided by the atomic number Z [7]. Adopting the recommended values for Hg and the scale with Z gives the values $RNT = 1.25 \cdot 10^{-8}$ and $H = 1.0 \cdot 10^{-2}$, which were used for the following calculations. $NNNP = 590$ is the default number of radial grid points which was adjusted to 2990 in order to fit all the radial functions used on the grid.

The exponential form of the distances is due to the radial functions having shorter wavelengths closer to the nucleus because of the higher kinetic energies. Higher densities of grid points are then useful to make good representations of the functions [6, p. 58]. The relatively high density of grid points near the nucleus also ensures that the shape of the radial charge distribution is probed thoroughly. Figure 5.2 shows that the radial grid captures the shape of the Fermi distribution used for the model of the nucleus in ^{199}Hg.

A finite difference scheme is used to approximate the MCDHF equations and to solve them on the numerical grid.

5.5 Obtaining Spectroscopic Orbitals

It is often difficult to obtain convergence while optimizing all radial functions simultaneously, especially when the system consists of a high number of electrons. Usually the spectroscopic orbitals are optimized with a small number of reference CSFs and are kept frozen during optimization of the virtual orbitals as the set of CSFs is expanded. In calculations on similar systems such as the states $6s6p\ ^3P_1$ in ^{201}Hg [15], and $5d^9 6s^2\ ^2D_{3/2}$ and $^2D_{5/2}$ in ^{197}Au [17], the minimal expansions have been used for the reference and the virtual orbitals have been added and optimized in layers. A layer of virtual orbitals, referred to as a virtual layer, is a set of virtual orbitals which contains no more than one orbital with the same quantum number κ. As

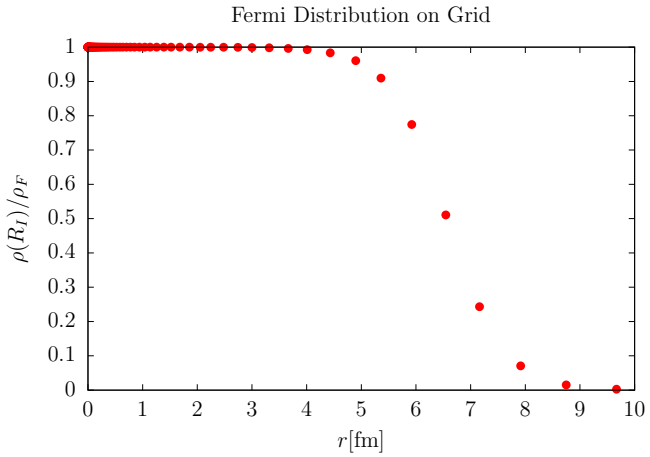

Figure 5.2: Normalized Fermi distribution calculated at radial grid points close to the nucleus.

the radial functions of each new layer are optimized, all previously obtained functions are kept frozen. A method similar to the one used for calculations in $6s6p\ ^3P_1$ in ^{201}Hg [15] was used for calculations on the states $6s6p\ ^3P_1$ and $6s6p\ ^3P_2$ in ^{199}Hg for this project.

The minimal expansion for the state $^3P_1$ included the CSFs corresponding to the relativistic configurations

$$6s_{1/2}6p_{1/2}$$
$$6s_{1/2}6p_{3/2}.$$

For the state $^3P_2$ the minimal expansion included only the CSF corresponding to the the relativistic configuration

$$6s_{1/2}6p_{3/2}.$$

All calculations were done separately for the two states. The radial functions for the spectroscopic orbitals were optimized simultaneously under the scf procedure with the minimal expansions. For the state $^3P_2$ this is technically not an MCDHF calculation but rather a Dirac-Hartree-Fock calculation since there is no configuration interaction. The initial estimates for the spectroscopic orbitals were obtained with the TF approximation.

5.6 Obtaining Virtual Orbitals

The virtual orbitals were added in layers by extending the CSF expansion to include CSFs generated by substitutions from a subset of the orbitals in the reference with orbitals in the new virtual layer. scf calculations were done where all new radial functions were optimized simultaneously while all previously optimized functions were kept frozen. Initial estimates for all new functions were obtained with the TF approximation.

The CSF expansions were in each case generated by all single as well as double vv and cv substitutions from the core subshells $5spd$ and valence subshells $6sp$ ($6p_{1/2}$ and $6p_{3/2}$ for $^3P_1$, and $6p_{3/2}$ for $^3P_2$) up to all new and previously obtained orbitals.

The program generates all CSFs with the same parity and total angular momentum as the reference within a set of rules specified by the user. Some of the generated CSFs may not be interacting with the reference by how the angular momenta are coupled and can be removed without much loss of precision [16, p. 42]. All CSFs not interacting with the reference CSFs through the DC Hamiltonian were therefore removed before the scf calculations were done.

After the scf calculations for each new virtual layer, a relativistic configuration interaction (RCI) was done where the transverse photon interaction from equation 4.26, vacuum polarization and self energy corrections were included. The scale factor for the transverse photon interaction was set to 10^{-6}. Self energy corrections were included for orbitals with principal quantum numbers $n \leq 6$. The CSF expansion was regenerated for the RCI where the Dirac-Coulomb-Breit operator was used for removal of non-interacting CSFs, leaving a somewhat higher number of CSFs in the resulting expansion than the DC Hamiltonian did. The hfs constant was calculated after each RCI. The addition of the 4^{th} virtual layer changed the calculated value by approximately 0.6 % and 0.5 % for the states $^3P_1$ and $^3P_2$, respectively, so no further layers were added. The compositions of the 4 virtual layers and the change in the value of the hfs constant from the preceding calculation can be viewed in Table 5.3.

For $^3P_2$ the 1^{st} virtual layer included both $6p_{1/2}$ and $7p_{1/2}$ which is an exception to the definition given for a virtual layer. The reason for this is that the $6p_{1/2}$ orbital was not included in the reference.

Virtual layer	Orbitals	$\delta A/A(^3P_1)[\%]$	$\delta A/A(^3P_2)[\%]$
1^{st}	$7s\ 7p\ 6d\ 5f\ 5g\ (6p_{1/2})$	24	12
2^{nd}	$8s\ 8p\ 7d\ 6f\ 6g\ 6h$	3.6	2.4
3^{rd}	$9s\ 9p\ 8d\ 7f\ 7g\ 7h$	3.4	3.2
4^{th}	$10s\ 10p\ 9d\ 8f\ 8g\ 8h$	-0.55	-0.50

Table 5.3: Orbitals included in the different virtual layers. The parentheses around orbital $6p_{1/2}$ indicates that it was included only for the $^3P_2$ state. $\delta A/A$ is the relative change in the hyperfine structure constant from the preceding calculation.

5.7 Obtaining the ASF

5.7.1 Single and Core-Valence Substitutions

The subshells lower in the core were opened for single and cv substitutions to the 4 virtual layers. The subshells were opened one by one in the order $4s \ldots 4f$ and then $3s \ldots 3d$. RCI and calculation of the hfs constant were performed after each new subshell had been opened.

The maximum number of orbitals in the AS that a CSF can be constructed from is limited by the program to 20. The maximum number of open relativistic core subshells is therefore 17 under the cv substitutions. In order to be able to study the effect of core subshells with $n < 3$, the $3d$ subshells were reclosed as the $2s$ and $1s$ subshells were opened for substitutions. The $2s$ and $1s$ subshells were reclosed for a calculation where the $2p$ subshells were opened. The changes in the calculated hfs constant relative to the preceding calculation as each subshell was opened are presented in Table 5.4.

When cc substitutions are to be included, the maximum number of open subshells is 16 due to the aforementioned limitation. The lowest contributing subshells w.r.t. the hfs constant were the $2p$, $3d$ and $3p$ subshells for both states. These subshells were therefore closed for substitutions in the further calculations. The contributions from each of these subshells were on the order of 0.1 % or less.

The significance of the different virtual orbitals were estimated by calculating the hfs constant for sets of CSFs generated by single, vv and cv substitutions from the subshells $1s2s3s4spdf5spd6sp$ to different subsets of the virtual orbitals. The smallest subset consisted of the virtual orbitals with

Subshell	$4s$	$4p$	$4d$	$4f$	$3s$
$\delta A/A[\%]$ $(^3P_1)$	1.2	0.34	0.37	2.0	0.43
$\delta A/A[\%]$ $(^3P_2)$	1.4	0.19	0.34	1.7	0.48
Subshell	$3p$	$3d$	$2s$	$2p$	$1s$
$\delta A/A[\%]$ $(^3P_1)$	0.13	0.040	0.29	0.085	0.24
$\delta A/A[\%]$ $(^3P_2)$	0.044	0.041	0.32	0.025	0.27

Table 5.4: Relative change from the preceding calculation in the value of the hyperfine structure constant as the core subshells were opened for single, vv and cv substitutions.

Virtual orbitals	$n = 5, 6$	$7s$	$7p$	$7d$	$7f$	$7g$	$7h$	$8s$	$8p$
$\delta A/A[\%](^3P_1)$	9.7	5.6	11	1.4	0.42	0.45	0.13	0.71	1.3
$\delta A/A[\%](^3P_2)$	-0.68	6.6	8.2	1.0	0.29	0.36	0.10	0.42	0.81
Virtual orbitals	$8d$	$8f$	$8g$	$8h$	$9s$	$9p$	$9d$	$10s$	$10p$
$\delta A/A[\%](^3P_1)$	0.31	0.14	0.20	0.15	2.6	0.80	-0.0077	-0.052	0.022
$\delta A/A[\%](^3P_2)$	0.22	0.10	0.16	0.12	3.1	0.37	0.14	0.11	0.00021

Table 5.5: Relative change in the hyperfine structure constant A from the preceding calculation as the virtual orbitals were included in the order $n = 5, 6, 7s \ldots 7h$ etc. with single, vv and cv substitutions.

$n = 5$ and $n = 6$. The set was extended by allowing substitutions up to one new orbital symmetry at a time in the order $7s \ldots 7h$, $8s \ldots 8h$, $9s \ldots 9d$, $10s$ and finally $10p$. The relative changes from from the preceding calculations are presented in Table 5.5.

The $10p$ orbitals were omitted from the AS in the further calculations for $^3P_2$ due to the very low contribution. Contributions from virtual orbitals not included are expected to be small from the trend of decreasing contributions with increasing principal and orbital quantum numbers. The resulting approximations then became the expansions generated by single, vv and cv substitutions from the subshells $1s2s3s4spdf5spd6sp$ to the virtual orbitals $5fg6(p_{1/2})dfgh7spdfgh8spdfgh9spd10s(p)$, which contained 65 443 and 62 211 CSFs for the states $^3P_1$ and $^3P_2$, respectively.

Virtual orbitals	$n = 5, 6$	$7s$	$7p$	$7d$	$7f$	$7g$	$7h$	$8s$
$\delta A/A[\%](^3P_1)$	-8.7	-1.4	-1.5	-1.3	-0.42	-0.39	-0.18	-0.18
$\delta A/A[\%](^3P_2)$	-4.3	-1.4	-0.94	-1.02	-0.30	-0.27	-0.12	-0.17
Virtual orbitals	$8p$	$8d$	$8f$	$8g$	$8h$	$9s$	$9p$	$9d$
$\delta A/A[\%](^3P_1)$	-0.72	-0.25	-0.080	-0.033	-0.22	0.014	-0.16	-0.089
$\delta A/A[\%](^3P_2)$	-0.50	-0.20	-0.086	-0.022	-0.15	0.00049	-0.13	-0.086

Table 5.6: Relative changes in the hyperfine constant A from the preceding calculation as the virtual orbitals were included in the order $n = 5, 6, 7s \ldots 7h$ etc. for cc substiutions from $5spd$.

5.7.2 Core-Core Substitutions

The CSF expansions from the approximations with single, vv and cv substitutions were extended further with cc substitutions. Double substitutions were first allowed from the core subshells $5spd$ to the AS where virtual orbitals with $n = 5$ and $n = 6$ were included. Virtual orbitals were then included in the order $7s \ldots 7h$ then $8s \ldots 8h$ etc. The relative changes from the preceding calculations are presented in Table 5.6.

The CSFs generated by cc substitutions from $5spd$ to $9spd8fgh$ were kept for $^3P_1$, and those from $5spd$ to $8s9sp8fgh$ were kept for $^3P_2$ along with the final expansions with the single, vv and cv approximations as the CSF expansion was extended further by including cc substitutions from the subshells $4spdf5spd$. The $9s$ virtual orbital was dropped for the state $^3P_2$ due to the low contribution. All CSFs generated up to this point were kept as the expansion was extended further using cc substitutions from lower core subshells.

The number of CSFs grows rapidly with inclusion of cc substitutions from $4spdf5spd$ and so only the virtual orbitals in the 1^{st} virtual layer, as defined in Table 5.3, were included in the first calculation. This reduced the value of the hfs constant by approximately 0.27 % for $^3P_1$ and 0.21 % for $^3P_2$. When also including the $3s$ subshell in the expansion the value was reduced further by approximately 0.0014 % for $^3P_1$ and increased by approximately 0.0021 % for $^3P_2$. cc substitutions from $3s$, or any of the lower subshells, were therefore not included for the further extension of the expansion.

Orbitals of the 2^{nd} virtual layer were included in the order $8sp7d6fgh$ and the hfs constant was calculated between each inclusion. The results are presented in Table 5.7.

Virtual orbitals	1^{st} layer	$8s$	$8p$	$7d$	$6f$	$6g$	$6h$
$\delta A/A[\%](^3P_1)$	-0.27	-0.11	-0.11	-0.26	-0.71	-0.23	-0.012
$\delta A/A[\%](^3P_2)$	-0.21	-0.11	-0.070	-0.18	-0.51	-0.15	-0.010

Table 5.7: Relative changes in the hyperfine constant A from the preceding calculation as the virtual orbitals were included in the order 1^{st} virtual layer, $8s$, $8p$, ..., $6h$. for cc substiutions from $4spdf5spd$.

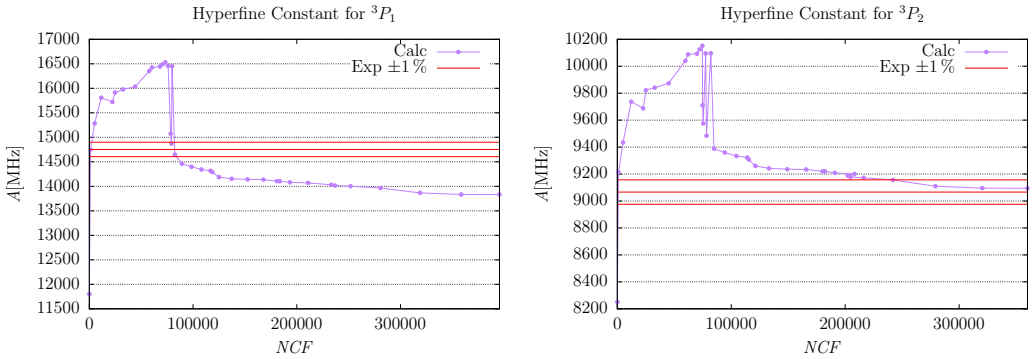

(a) $^3P_1$ (b) $^3P_2$

Figure 5.3: Calculated values of the hyperfine constant A with increasing CSF expansions. The red lines show the experimental values ±1 %.

At this point the contributions from the CSFs not included in the expansion were considered to be less than a percent. The graphs in Figure 5.3 show the calculated values of the hfs constant as the set of CSFs was extended for each of the states. It can be seen that the use of single, vv and cv substitutions resulted in an overshooting of the hfs value while the use of cc substitutions relaxed this overshooting. The graphs show similarities with the one obtained for ^{201}Hg by Bieroń et al. [15] except for it being reflected around the horizontal axis due to the gyromagnetic ratio of ^{201}Hg having opposite sign. For the state $^3P_2$ the value converges within 1 % of the experimental value. For $^3P_1$ the value seems to converge, but toward a value that is approximately 6 % lower than the experimental value. The final expansions consisted of 395 461 CSFs for $^3P_1$ and 359 985 CSFs for $^3P_2$.

Chapter 6

Paramteric Study of the Breit-Rosenthal Effect between ^{199}Hg and other isotopes

6.1 Variation in the Mean Squared Radius

The chart of nuclei from IAEA [13] lists the isotopes from ^{171}Hg to ^{216}Hg. Extrapolation of the data over nuclear radii [12] gives estimated differences in the mean squared radius of approximately $\pm 1\,\mathrm{fm}^2$ from ^{199}Hg to the lower and upper extremes in the chart of nuclei for Hg. This range in mean squared radius was used in the parametric study for estimation of the factor C in the linear fit $C\delta\langle r_n^2\rangle$ for the approximation of the BR effect as described in section 3.4.

Using the final CSF expansions obtained for ^{199}Hg in the previous chapter, all radial functions and expansion coefficients were recalculated for the ASFs for both states with values of the nuclear mean squared radius at increments of $0.2\,\mathrm{fm}^2$ in both directions from that used for ^{199}Hg. The nuclear skin thickness was kept constant. The results are presented in Table 6.1 and Figure 6.1. Results from the corresponding calculations with the minimal CSF expansions are presented in Table 6.2 and Figure 6.2.

The proportionality constant C from the linear fit $C\delta\langle r_n^2\rangle$ is found by linear regression with a so-called no-intercept model where the intercept with the vertical axis is forced through the origin. With the data points obtained in each of the cases the expression for the constant C becomes [3]

$\delta\langle r_n^2\rangle$[fm^2]	-1	-0.8	-0.6	-0.4	-0.2
$\delta A/A_0$[%] ($^3P_1$)	0.1126	0.089 89	0.067 26	0.044 73	0.022 31
$\delta A/A_0$[%] ($^3P_2$)	0.1146	0.090 21	0.065 90	0.053 62	0.024 90
$\delta\langle r_n^2\rangle$[fm^2]	0.2	0.4	0.6	0.8	1
$\delta A/A_0$[%] ($^3P_1$)	-0.022 21	-0.044 32	-0.066 33	-0.088 24	-0.1101
$\delta A/A_0$[%] ($^3P_2$)	-0.029 46	-0.046 71	-0.070 35	-0.093 91	-0.1173

Table 6.1: Relative change in the hyperfine structure constant $\delta A/A_0$ with variation in the mean squared radius of the nuclear charge distribution $\delta\langle r_n^2\rangle$ from the reference nucleus with hyperfine structure constant A_0 in the electronic states $^3P_1$ and $^3P_2$ with the largest expansions.

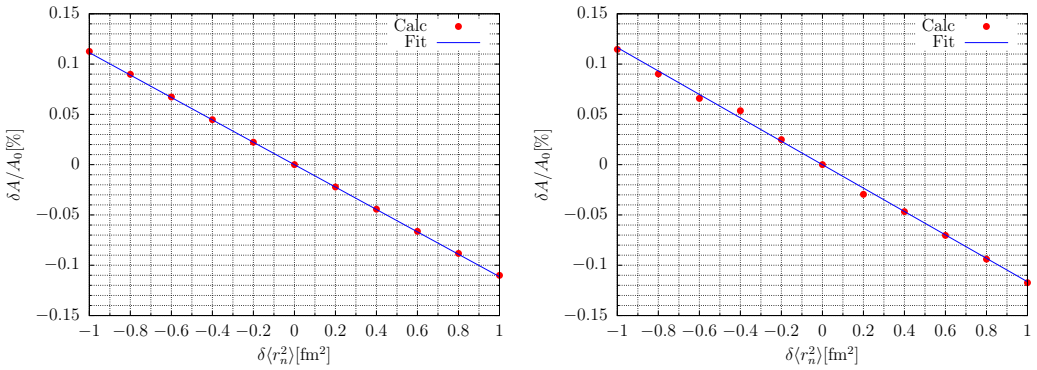

(a) $^3P_1$ (b) $^3P_2$

Figure 6.1: Relative change in the hyperfine structure constant $\delta A/A_0$ with variation in the mean squared radius of the nuclear charge distribution $\delta\langle r_n^2\rangle$ from the reference nucleus with hyperfine structure constant A_0 in the electronic states $^3P_1$ and $^3P_2$ with the largest expansions. The blue line represents the linear fit $C\delta\langle r_n^2\rangle$.

$\delta\langle r_n^2\rangle$[fm^2]	-1	-0.8	-0.6	-0.4	-0.2
$\delta A/A_0$[%] ($^3P_1$)	0.1119	0.089 30	0.066 81	0.044 44	0.022 16
$\delta A/A_0$[%] ($^3P_2$)	0.1210	0.096 56	0.072 25	0.048 05	0.023 97
$\delta\langle r_n^2\rangle$[fm^2]	0.2	0.4	0.6	0.8	1
$\delta A/A_0$[%] ($^3P_1$)	$-0.022\,07$	$-0.044\,03$	$-0.065\,89$	$-0.087\,66$	-0.1093
$\delta A/A_0$[%] ($^3P_2$)	$-0.023\,83$	$-0.047\,61$	$-0.071\,25$	$-0.094\,79$	-0.1182

Table 6.2: Relative change in the hyperfine structure constant $\delta A/A_0$ with variation in the mean squared radius of the nuclear charge distribution $\delta\langle r_n^2\rangle$ from the reference nucleus with hyperfine structure constant A_0 in the electronic states $^3P_1$ and $^3P_2$ with the minimal expansions.

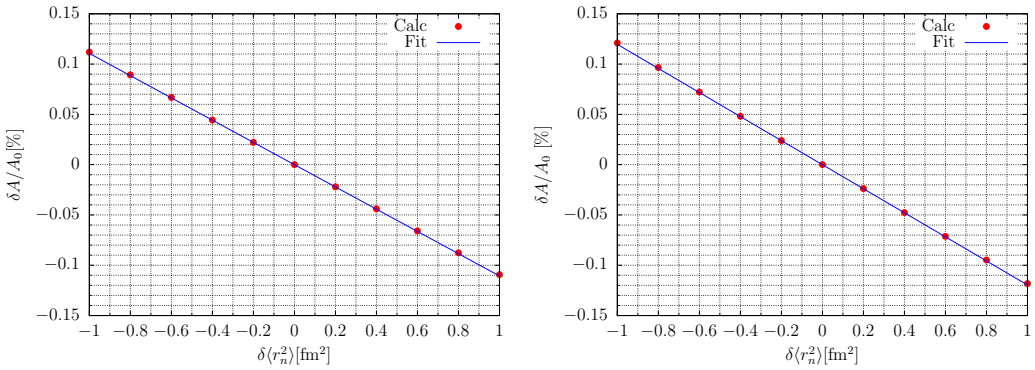

(a) $^3P_1$ (b) $^3P_2$

Figure 6.2: Relative change in the hyperfine structure constant $\delta A/A_0$ with variation in the mean squared radius of the nuclear charge distribution $\delta\langle r_n^2\rangle$ from the reference nucleus with hyperfine structure constant A_0 in the electronic states $^3P_1$ and $^3P_2$ with the minimal expansions. The blue line represents the linear fit $C\delta\langle r_n^2\rangle$.

State	Largest		Minimal	
	$C[\%\,\mathrm{fm}^{-2}]$	R_0^2	$C[\%\,\mathrm{fm}^{-2}]$	R_0^2
$^3P_1$	-0.1113	0.9999	-0.1106	0.9999
$^3P_2$	-0.1164	0.9980	-0.1196	0.9999

Table 6.3: The proportionality constant C in the linear fit $C\langle r_n^2\rangle$ for the BR effect along with the corresponding coefficients of correlation R, up to 4 digits, for the states $^3P_1$ and $^3P_2$ with both the largest and minimal expansions.

$$C = \frac{\sum_i x_i y_i}{\sum_i x_i^2}, \tag{6.1}$$

where x_i represent the values of $\delta\langle r_n^2\rangle$ and y_i represent the values of $\delta A/A_0$ at the respective data points.

The coefficient of determination for the no-intercept model, R_0^2 (distinguished from the R^2 for the model with interception term), is given by [3]

$$R_0^2 = \frac{\sum_i \hat{y}_i^2}{\sum_i y_i^2} = \frac{C^2 \sum_i x_i^2}{\sum_i y_i^2}, \tag{6.2}$$

where $\hat{y}_i$ is the value predicted by the no-intercept model at x_i. The coefficient of determination is a measure of how well the linear fit approximates the data points. It takes values in the range $[0, 1]$. The closer the value is to 1, the better the fit approximates the data which in turn is interpreted as a measure on how well $C\delta\langle r_n^2\rangle$ represents the BR effect.

6.2 Variation in Nuclear Skin Thickness

Variation in the nuclear skin thickness with the mean squared radius kept constant corresponds to variations in the higher radial moments of the nuclear charge distribution. Calculations of the hfs constant for such variations indicate how much the higher order radial moments contribute to the BR effect and to which degree the linear fit could be expected to be valid for the different isotopes.

The two parameter Fermi charge distribution has been fitted to scattering data [5, pp. 31–36]. It was found that the skin thickness was approximately constant for nuclei with mass number $A > 16$ with a standard deviation of 0.1 fm.

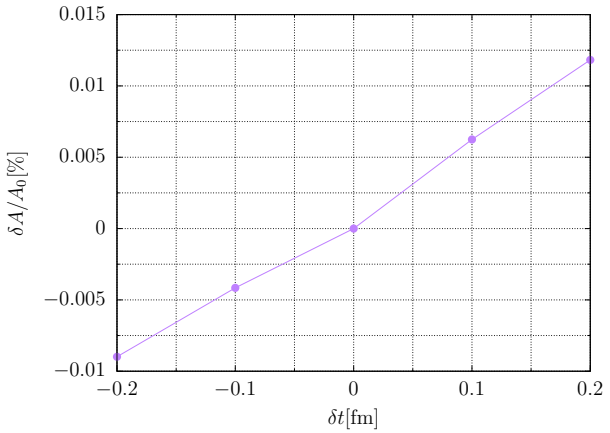

Figure 6.3: Relative change in the calculated hyperfine constant for the state $^3P_2$ with changes in skin thickness δt from the reference model ($t = 2.3\,\text{fm}$). The mean squared radius was kept constant.

For the state $^3P_2$, new series of calculations on the hfs constant were made where the values 2.1 fm, 2.2 fm, 2.4 fm and 2.5 fm were used for the nuclear skin thickness. These values correspond to using 1 and 2 standard deviations from the previously mentioned results above and below the standard value 2.3 fm used by GRASP2018. This range was considered to be a conservative estimate of how much the nuclear skin thickness could be expected to differ from the standard value for the isotopes of Hg. For each of the values of the nuclear skin thickness, calculations were done with $\delta\langle r_n^2\rangle$ in the range $[-1\text{fm}^2, 1\text{fm}^2]$ in increments of $0.25\,\text{fm}^2$.

The variation in the calculated hfs constant for different skin thickness, where the mean squared radius was kept constant and equal to the one used for the reference model, can be seen in Figure 6.3. The variation in the hfs constant for different values of the mean squared radius for each of the values used for the skin thickness can be seen in Figure 6.4. The corresponding values of the proportionality constant C in the linear fit and the coefficient of determination R_0^2 can be seen in Table 6.4.

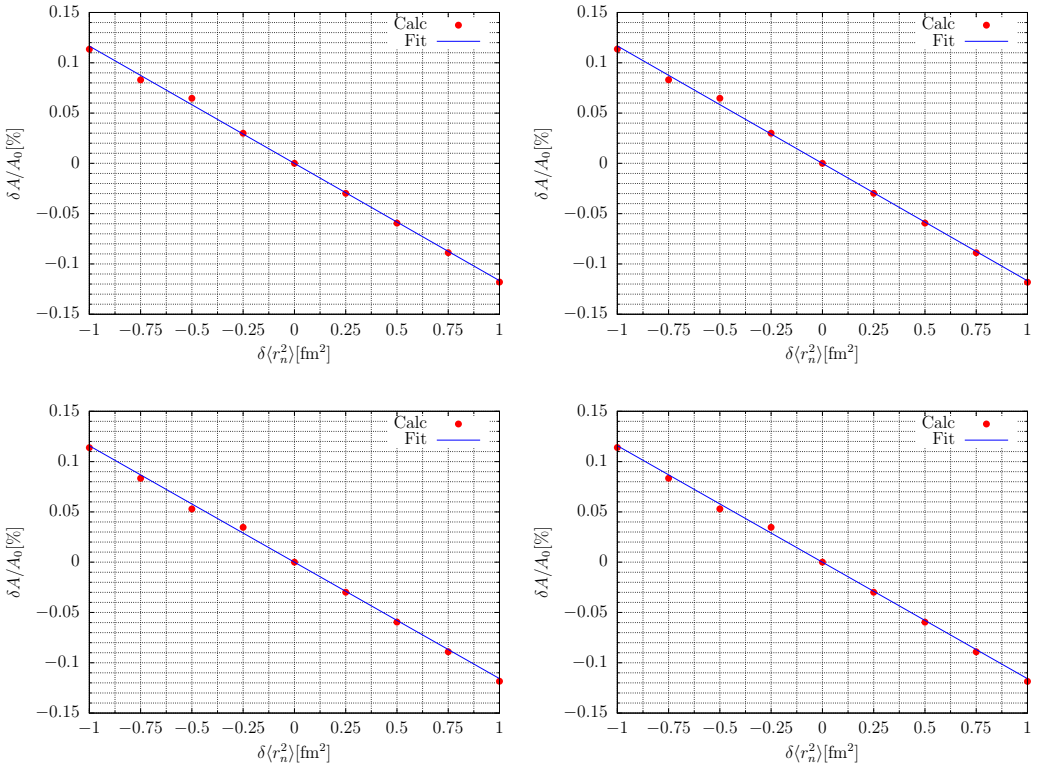

Figure 6.4: Relative change in the hyperfine structure constant $\delta A/A_0$ with variation in the mean squared radius of the nuclear charge distribution $\delta\langle r_n^2\rangle$ from the reference nucleus with hyperfine structure constant A_0 in the electronic $^3P_2$ with the largest expansion. In the order from upper left to lower right plot (horizontally) the values of skin thickness were 2.1 fm, 2.2 fm, 2.4 fm and 2.5 fm. The blue line represents the linear fit $C\delta\langle r_n^2\rangle$.

δt[fm]	C[% fm^{-2}]	R_0^2
−0.2	−0.1166	0.9985
−0.1	−0.1167	0.9985
0	−0.1164	0.9980
0.1	−0.1157	0.9983
0.2	−0.1158	0.9982

Table 6.4: Calculated proportionality constant C in the linear fit $C\delta\langle r_n^2\rangle$ and corresponding coefficients of determination R_0^2 for different skin thickness deviations δt from the reference model ($t = 2.3\,\text{fm}$).

6.3 Discussion

6.3.1 Variation in Mean Squared Radius

The calculated values of the constant C can be compared with the results in Tl [2] where the corresponding value of the factor C can be estimated with the average of the results that is presented for the relativistic states $7s$ and $6p_{1/2}$. This gives $C(\text{Tl}) \approx -0.09\,\%\,\text{fm}^{-2}$. The values obtained for Hg is close to the value for Tl which was calculated with more advanced methods, indicating that the results are reasonable.

For each of the electronic states, the calculated proportionality constant C using the minimal expansion was quite similar to that calculated with the largest expansion. The largest difference was for $^3P_2$ where the value increased (absolute value decreased) by approximately 2.7 % from the minimal to the largest expansion. For $^3P_1$ the value decreased (absolute value increased) by approximately 0.67 %. This indicates that large CSF expansions and the associated large computational efforts may not be necessary for calculation of the BR effect unless even higher precision is needed.

For the minimal expansions the only orbitals contributing to the magnetic hyperfine interaction are the valence orbitals since all other subshells are closed which give net contributions of 0 to the interaction energy. The largest expansions include CSFs with open core subshells which contribute to the hyperfine interaction, which was described with core polarization under sections 5.3.1 and 5.3.2. The BR effect is expected to mostly depend on the $s_{1/2}$ and $p_{1/2}$ orbitals since these are the only ones with non-zero probability densities at the nuclear center which is required for the first order corrections to the BR correction in equation 3.21. The small difference in C between

the minimal and largest expansion indicates that the BR effect is mostly unaffected by the principal quantum number n for the $s_{1/2}$ and $p_{1/2}$ subshells that contribute to the hyperfine interaction.

The BR effect between ^{199}Hg and other relatively stable isotopes, predicted with the obtained values of the constant C, can be compared with known hyperfine anomalies to see the significance of the BR effect. The isotopes ^{197}Hg and ^{195}Hg have angular momentum $I = 1/2$, similar to ^{199}Hg. From the table over experimentally obtained nuclear rms radii [12], the differences in mean squared radius become $\delta\langle r_n^2\rangle_{197,199} \approx -0.0675\,\mathrm{fm}^2$ and $\delta\langle r_n^2\rangle_{195,199} \approx -0.140\,\mathrm{fm}^2$, respectively. The hyperfine anomalies are known for the state $6s6p\ ^3P_1$ between ^{199}Hg and these isotopes [23]. The values are $^{197}\Delta^{199} = 0.0778(7)\,\%$ and $^{195}\Delta^{199} = 0.1470(9)\,\%$. With the value C obtained with the largest expansion for $^3P_1$ (Table 6.3) the BR corrections are approximately $0.007\,51\,\%$ and $0.0156\,\%$ respectively. The BR effect is therefore expected to make up around $10\,\%$ of the hyperfine anomaly for these cases. The uncertainty in the ratio of the nuclear gyromagnetic ratios associated with the hyperfine anomaly can then be reduced by around $10\,\%$ for similar cases.

The differences in mean squared radius from ^{199}Hg are however expected to be significantly larger for unstable isotopes (largest on the neutron-rich side). For isotopes with the same angular momentum I and similar values of the magnetic moment μ_I, and with larger differences in the mean squared radius, the BR effect can be expected to make up even more of the hyperfine anomaly.

As an example with Eu, the hyperfine anomaly between ^{151}Eu and ^{145}Eu and between ^{151}Eu and ^{147}Eu are relatively small, $-0.08(15)\,\%$ and $-0.12(17)\,\%$, respectively [23]. The differences in mean squared radius are $\delta\langle r_n^2\rangle_{151,145} = 0.8606\,\mathrm{fm}^2$ and $\delta\langle r_n^2\rangle_{151,147} = 0.5867\,\mathrm{fm}^2$ [12]. Considering the BR effect with the factor C on the order of $-0.5\,\%\,\mathrm{fm}^{-2}$ for Eu indicates that the contribution to the total hyperfine anomaly is higher than $10\,\%$. Note that the angular momenta are the same and that the magnetic moments are almost the same for these isotopes which is why the BW effect is small.

6.3.2 Variation in Skin Thickness

The results in Figure 6.3 were obtained with a conservative estimate on how much the nuclear skin thickness could be suspected to differ from the standard value 2.3 fm. The largest deviation in the calculated value of the

hfs constant was approximately 0.012 % where the value of the skin thickness was 0.2 fm larger than the reference value. This difference in the hfs constant is on the order of 10 % of the BR effect when $\delta\langle r_n^2\rangle$ is about $\pm 1\,\mathrm{fm}^2$. At these ranges the precision of the calculated BR effect can at least be expected to be within 10 %.

The calculated values of the proportionality constant C in the linear fit $C\delta\langle r_n^2\rangle$ with different values of the skin thickness are very similar. The smallest value (largest absolute value) is approximately 0.88 % smaller than the largest (smallest absolute value).

These results indicate that the value of the skin thickness does not have much impact on the BR effect as long as the skin thickness is very similar for the isotopes. However, if the skin thickness differs between the isotopes, this could have a higher impact on the hfs constant and thus reduce the accuracy of the linear fit for the BR effect. If the variation in skin thickness is smaller than 0.1 fm the impact is expected to be less than 5 % of the BR effect when the difference in mean squared radius is about $\pm 1\,\mathrm{fm}^2$.

Chapter 7

Conclusion

The Breit-Rosenthal effect between ^{199}Hg and different isotopes has been calculated in a parametric study where the difference in the mean squared radius of a two-parameter Fermi nucleus was varied and the hyperfine structure constant was calculated numerically for the states $^3P_1$ and $^3P_2$ in the configuration $6s6p$. The electronic wave functions were calculated with the multiconfiguration Dirac-Hartree-Fock method. Calculations were done with the General Relativistic Atomic Structure Package 2018.

A linear fit on the form $C\delta\langle r_n^2\rangle$ was assumed and the factor C was calculated from the results of the parametric study. The difference in the value of C between the minimal configuration expansion and an expansion with ~ 400000 configurations was found to be on the order of 1 % indicating that a large expansion may not be needed for calculations of the Breit-Rosenthal effect. Differences in the Fermi model skin thickness was found to have a smaller impact on the hyperfine structure constant. With the largest expansions the values for the constant C for the range $\delta\langle r_n^2\rangle \in [-1\text{fm}^2, 1\text{fm}^2]$ were found to be $-0.1113\,\%\,\text{fm}^{-2}$ for $^3P_1$ and $-0.1164\,\%\,\text{fm}^{-2}$ for $^3P_2$.

With these results the Breit-Rosenthal effect is estimated to make up around 10 % of the hyperfine anomalies $^{199}\Delta^{197}$ and $^{199}\Delta^{195}$ for Hg. For isotopes with larger differences in mean squared radius of the charge distribution, while the angular momenta and magnetic moments are similar, it is expected that the Breit-Rosenthal effect could contribute even more than 10 % to the hyperfine anomaly.

Bibliography

[1] Mårtensson-Pendrill A-M. "Atoms through the looking glass - a relativistic challenge". In: *Canadian Journal of Physics* 86.1 (2008), pp. 99–109. DOI: 10.1139/P07-116.

[2] Mårtensson-Pendrill A-M. "Magnetic Moment Distributions in Tl Nuclei". In: *Physical Review Letters* 74.12 (1995), pp. 2184–2187. DOI: https://doi.org/10.1103/PhysRevLett.74.2184.

[3] Kozak A and Kozak R A. "Notes on regression through the origin". In: *The Forestry Chronicle* 71.3 (1995), pp. 326–330.

[4] Preston M A and Bhaduri R K. *Structure of the Nucleus*. Reading Massachusetts 01867, U.S.A.: Addison-Wesley Publishing Company, Inc., 1975. ISBN: 0201059762.

[5] Elton L R B. *Nuclear Sizes*. Oxford University Press, 1961.

[6] Froese Fischer C, Brage T, and Jönsson P. *Computational Atomic Structure*. Institute of Physics Publishing, 1997. ISBN: 0750304669.

[7] Froese Fischer C et al. "GRASP2018 - A Fortran 95 version of the General Relativistic Atomic Structure Package". In: *Comput. Phys. Commun. (in preses 2018)* 237.April (2019), pp. 184–187. DOI: https://doi.org/10.1016/j.cpc.2018.10.032.

[8] Cowan R D. *The Theory of Atomic Structure and Spectra*. University of California Press, 1981. ISBN: 0520038215.

[9] Dyall K G et al. "GRASP: A General-Purpose Relativistic Atomic Structure Program". In: *Computer Physics Communications* 55 (1989), pp. 425–456. DOI: https://doi.org/10.1016/0010-4655(89)90136-7.

[10] Olsson G. *Hyperfine-Structure Investigations of Atoms with Two Open Shells*. Department of Physics Göteborg, 1982.

[11] Griffiths. "Hyperfine splitting in the ground state of hydrogen". In: *Am. J. Phys* 50.8 (1982), pp. 698–703.

[12] Angeli I and Marinova K P. "Table of experimental nuclear ground state charge radii: An update". In: *Atomic Data and Nuclear Data Tables* 99.1 (2013), pp. 69–95. DOI: https://doi.org/10.1016/j.adt.2011.12.006.

[13] *IAEA Live Chart of Nucleides*. URL: https://nds.iaea.org/relnsd/vcharthtml/VChartHTML.html. (accessed: 29.05.2020).

[14] *IAEA Nuclear Electromagnetic Moments*. URL: https://www-nds.iaea.org/nuclearmoments. (accessed: 02.05.2020).

[15] Bieroń J, Jönsson P, and Pekka Pyykö. "Nuclear quadrupole moment of 201Hg". In: *Physical Review A* 71.1 (2005). DOI: https://doi.org/10.1103/PhysRevA.71.012502.

[16] Bieroń J et al. *A practical guide to GRASP2018 - A collection of Fortran 95 programs with parallel computing using MPI*. Computational Atomic Structure Group. 2018.

[17] Bieroń J et al. "Complete-active-space multiconfiguration Dirac-Hartree-Fock calculations of hyperfine-structure constants of the gold atom". In: *Physical Review A* 79.5 (2009). DOI: https://doi.org/10.1103/PhysRevA.79.052502.

[18] D F Jackson Kimball. "Nuclear spin content and constraints on exotic spin-dependent couplings". In: *New Journal of Physics* 17.7 (July 2015), p. 073008. DOI: 10.1088/1367-2630/17/7/073008. URL: https://doi.org/10.1088%2F1367-2630%2F17%2F7%2F073008.

[19] McDermott M N and Lichten W L. "Hyperfine Structure of the 6^3P_2 State of $_{80}Hg^{199}$ and $_{80}Hg^{201}$. Properties of Metastable States of Mercury". In: *Physical Review* 119.1 (1960). DOI: https://doi.org/10.1103/PhysRev.119.134.

[20] Grant I P. *Relativistic Quantum Theory of Atoms and Molecules*. Springer, 2007.

[21] Jönsson P et al. "New Version: GRASP2K relativistic atomic structure package". In: *Computer Physics Communications* 184.9 (2013), pp. 2197–2203. DOI: https://doi.org/10.1016/j.cpc.2013.02.016.

[22] Schwerdtfeger P et al. “Relativistic and quantum electrodynamic effects in superheavy elements”. In: *Nuclear Physics A* 944.December (2015), pp. 551–577. DOI: https://doi.org/10.1016/j.nuclphysa.2015.02.005.

[23] Persson J R. “Table of hyperfine anomaly in atomic systems”. In: *Atomic Data and Nuclear Data Tables* 99.1 (2013), pp. 62–68. DOI: https://doi.org/10.1016/j.adt.2012.04.002.

[24] Büttgenbach S. “Magnetic Hyperfine Anomalies”. In: *Hyperfine Interactions* 20.1 (1984), pp. 1–64. DOI: https://doi.org/10.1007/BF02043319.

[25] Stager C V. “Hyperfine Structure of Hg^{197} and Hg^{199}”. In: *Physical Review* 132.1 (1963). DOI: https://doi.org/10.1103/PhysRev.132.275.

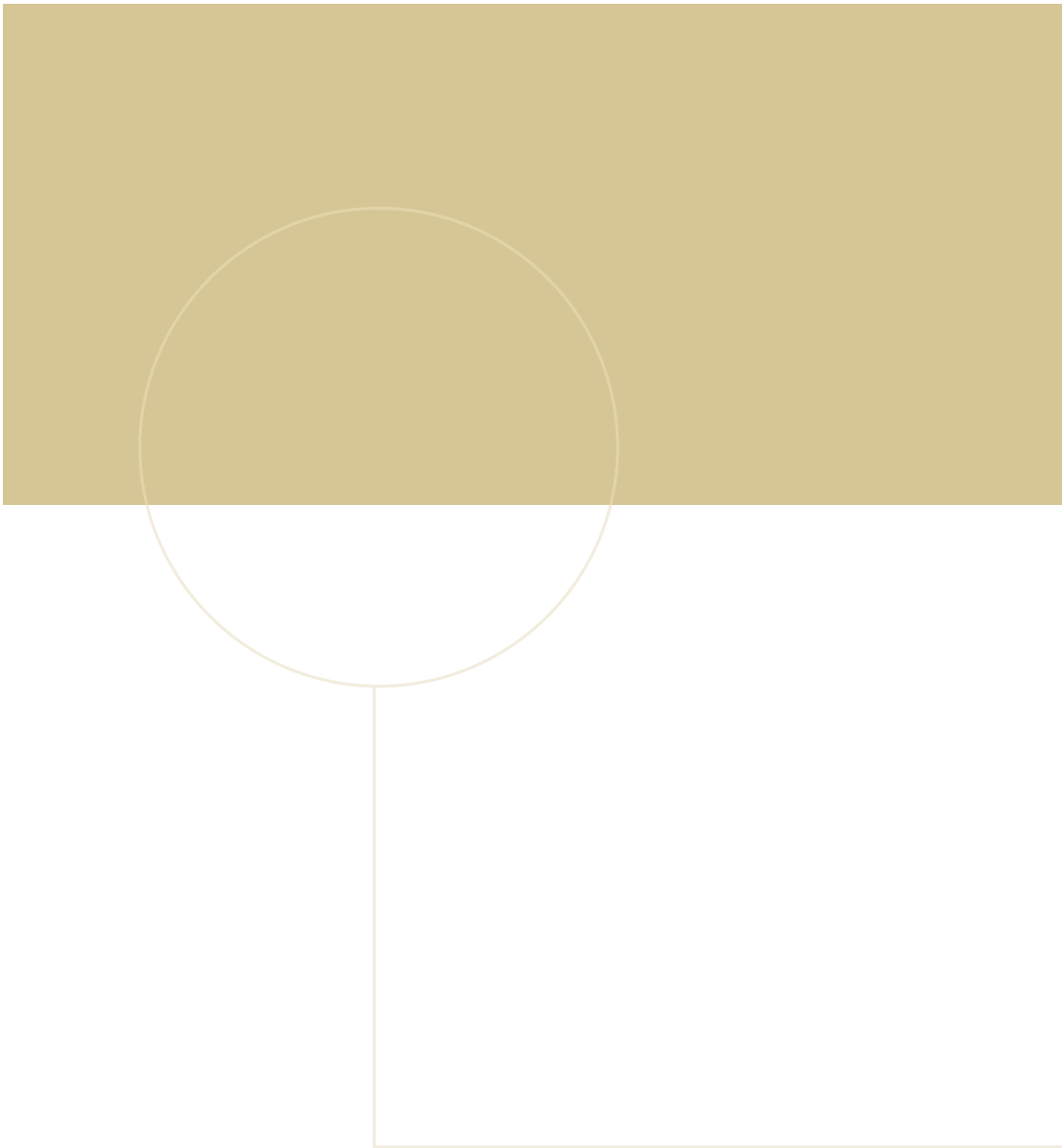

NTNU

Kunnskap for en bedre verden